Indirect Detection of γ Rays Using a Complete Kinematics Approach

Martin Weigand

201705072

Master's Thesis in Physics

February 2023

Supervisor: Hans Fynbo

Department of Physics and Astronomy

Aarhus University

Abstract

This thesis aimed to explore the use of the Indirect Detection Of Gamma rays (IDOG) method in detecting electromagnetic transitions in γ-delayed particle emissions in ^{16}O and ^{8}Be.

For ^{16}O, the objective was to determine if natural parity states above the α separation energy, and in particular the 9.59 (1^-) and 9.84 (2^+) MeV states, could be populated through the γ-delayed α-decay of the 12.97 (2^-) and 13.09 (1^-) MeV states in ^{16}O. To investigate this, two ^{15}N(p,α)^{12}C experiments were carried out at the Van der Graaf accelerator at the Department of Physics and Astronomy at Aarhus University with laboratory beam energies of 902 and 1028 keV. Using the IDOG method, the study found no significant amount of γ-delayed α-decay to any of the natural parity states. Instead, using Monte Carlo simulation, it was possible to set sensible 90% CL upper limits on the radiative decay widths, which for the 12.97 $\rightarrow$ 9.84, 12.97 $\rightarrow$ 9.59, 13.09 $\rightarrow$ 9.84, and 13.09 $\rightarrow$ 9.59 dipole transitions gave upper limits of 7.5 meV, 21 meV, 0.12 eV and 0.25 eV, respectively.

For ^{8}Be, the objective was to perform a feasibility study of using the IDOG method on a ^{10}B(d,α)^{8}Be experiment to measure the γ spectrum for the transitions from the isospin doublet (2^+) to the broad 3.0 (2^+) MeV state in ^{8}Be. This was done using Monte Carlo simulations of the γ-delayed 2α breakup and comparing γ spectra generated with the IDOG method to theoretical spectra from the simulations. This comparison revealed systematic uncertainties associated with energy loss corrections and response function, which must be addressed in extracting a reliable R-matrix parameterization of an IDOG-generated γ spectrum in an actual ^{10}B(d,α)^{8}Be experiment. These results lay the foundation for further work with this experiment.

Acknowledgements

First and foremost, I extend my gratitude to my supervisor Hans Fynbo and co-supervisor Karsten Riisager for their supervision and guidance throughout the journey of this thesis. My experience working in the Aarhus Subatomic group has been a memorable one, providing both personal and academic growth.

I would also like to express my deep appreciation to Erik Asbjørn Mikkelsen Jensen for his unwavering patience in answering my countless questions and for providing much-needed support in resolving my many hair-tearing software issues. Without his assistance, this thesis would not have been possible.

I would also like to thank all my office mates at 1520-821 for their support and for providing a pleasant work environment during the past year.

Finally, I would like to thank my family and partner for their love, support and constant encouragement. I will forever be grateful for their belief in me.

Martin Weigand
Aarhus, February 2023

Contents

Chapter 1

Introduction

The concept of atoms has been around since ancient times, but it wasn't until the former half of the 19th century that scientists applied the methods of experimental science to the problem and from their studies provided evidence that matter is indeed made up of atoms [1]. A century later, Ernest Rutherford conducted a series of famous experiments known as the 'gold foil' experiments which aimed to investigate the structure of atoms. Together with previous studies of Becquerel, Curie, and Thomson, the nuclear model of an atom was proposed. In this model, negatively charged particles called electrons revolve around a small, dense nucleus containing positively charged particles, which got called protons. Furthermore, the existence of neutrally charged particles in the nucleus were announced in the 1930s. These got called neutrons and introduced the concept of isotopism: elements can have various numbers of neutrons in the nucleus which breaks the degeneracy of properties and behavior in elements [2]. All the discoveries mentioned above and the development of quantum mechanics had a profound impact on the study of atoms. These advances led to the emergence of a new field of study known as nuclear physics, which focused specifically on the properties and behavior of atomic nuclei.

Today we know that protons and neutrons are not elementary particles, but are manifestations of more fundamental particles called quarks. In this quark model, each proton and neutron is made up of three quarks, which are held together by the strong nuclear force, mediated by a force-carrying particle denoted as the gluon. The interactions between quarks and gluons are

described within the theoretical framework of Quantum ChromoDynamics (QCD). However, the complexity and mathematical difficulty of QCD, combined with the challenges of experimentally studying the behavior of quarks and gluons and the behavior of the strong force, make QCD a difficult theory to use when studying atomic nuclei [1].

Instead, much of the richness of our knowledge of nuclear physics largely depends on what we know from studying electromagnetic and weak transitions of excited states in nuclei through nuclear reaction experiments. The theories describing the corresponding forces of these transitions are better understood and in general easier to work with than QCD, resulting in more reliable matrix elements. Thus these are excellent probes to study nuclear properties and structure.

In particular, electromagnetic transitions have extensively been used to study the excitation spectra of elements. In these, a nucleus in an excited state transition into a lower-lying excited state or the ground state by emitting a photon. These are called γ rays and their energy is measured with γ spectroscopy conventionally using scintillation or semiconductor detectors.

The focus of this thesis will be on electromagnetic transitions in nuclei involving particle unbound excited states. The latter is nuclear states in which it is energetically possible for the nucleus to decompose into smaller nuclei, making them very short-lived and hence having very broad energy profiles. Accordingly, electromagnetic transitions involving unbound states lead to broad energy distributions of the emitted γ rays. In this situation, conventional γ-spectroscopy of electromagnetic transitions has presented itself as insufficient to provide useful spectra due to both the wide energy range in a conventional detectors response function and also the small γ branches in unbound states, caused by the large probability to break up into smaller nuclei. This thesis will explore an alternative experimental approach referred to as the IDOG method: Indirect Detection Of Gamma rays. In this method, the conventional direct detection of γ-rays is substituted with indirect detection through measurements of multi-particle breakups in so-called complete kinematics. What this exactly means will be elucidated further in the thesis.

1.1 Aim and structure of this thesis

This thesis is going to work as a case study, revolving around two cases in which it could be advantageous to use the IDOG method. These are the γ-delayed α-decay of ^{16}O and the γ-delayed 2α breakup of ^{8}Be, which both are relevant for the field of nucleosynthesis. Specifically, the aim of studying these cases is:

1. To use the IDOG method on data from an ^{15}N(p,α)^{12}C experiment to determine radiative decay widths of the 12.97 (2^-) and 13.09 (1^-) MeV states to excited states above the α separation energy in ^{16}O.

2. To use Monte Carlo simulations to perform a feasibility study of using the IDOG method on a ^{10}B(d,α)^{8}Be experiment to measure the γ spectrum for the transitions from the isospin doublet (2^+) to the broad 3.0 (2^+) MeV state in ^{8}Be.

In addition to these two goals, this thesis will also work as a proof of concept of the IDOG method and discuss some of the methodological aspects regarding the method itself. Consequently, a third aim of this thesis is:

3. To demonstrate the IDOG method through the two cases mentioned above.

The thesis will be structured as follows:

- In Chapter 2 I will introduce the theoretical framework that I will be working in, including a brief overview of conventional γ spectroscopy and its limitations in measuring electromagnetic transitions involving unbound states. This will then lead to an introduction of the IDOG method.
- In Chapter 3 and Chapter 4 I will present the work related to the γ-delayed α decay of ^{16}O and the γ-delayed 2α breakup of ^{8}Be, respectively. They will include their own motivation and final discussion. Since many of the methodological and analytical aspects are similar, these will only be introduced in Chapter 3, with Chapter 4 referring to relevant sections in Chapter 3.
- In Chapter 5 I will summarise the work presented in this thesis in a conclusion.

Chapter 2

Theoretical framework

Nuclear physics lacks a coherent, unified theoretical formulation capable of explaining all observed nuclear phenomena on a fundamental level. Thus we are left with trying to explain them through the ontological concept of structural realism in which we accept that the phenomena are only described by scientific theories but their underlying nature is yet uncertain.

2.1 Nuclear structure

In the case of nuclear structure, there are several theories that have been developed since the former half of the 20th century. A comprehensive description of the various nuclear structure theories is given in [3]. I will mention a few of them here.

One of the first nuclear structure theories to be described was the liquid drop model. It originates from the observed feature that nuclei have nearly uniform inner density. This model ultimately leads to the semi-empirical-mass-formula which is fairly successful at parameterizing the binding energy per nucleon of different isotopes.

It turns out that nuclei with a magic number of neutrons or protons are significantly more stable than predicted by the liquid drop model. The first seven nuclear magic numbers are

$$\text{Magic numbers:} \quad 2,\ 8,\ 20,\ 28,\ 50,\ 82,\ 126.$$

This feature is explained within the nuclear shell model. This treats each nucleon as moving in a mean-field potential generated by the other nucleons in the nuclei. Using a Woods-Saxon potential with a spin-orbit term as the mean-field potential, clustered discrete single-particle energy levels emerge, creating shell structures as seen in atomic physics. These are then filled according to the Pauli exclusion principle. Just like the noble gasses being the most stable due to their outermost occupied shell being filled, the magic numbers correspond to closed shell configurations, such that the last nucleon in a closed shell is more strongly bound than the following 'valence' nucleons. Additionally, protons and neutrons tend to pair up so that each pair has a spin of zero and even parity. For even-even nuclei, this results in the predicted spin-parity of the ground state being 0^+.

Nuclei with a magic number of both protons and neutrons are called doubly magic and are particularly stable. An important doubly magic nucleus is the α particle, ^{4}He. In fact, it turns out that the binding energy per nucleon is the highest for α-conjugate nuclei, i.e. nuclei that are multiples of α (^{8}Be, ^{12}C, ^{16}O, ^{20}Ne etc.). This led to the idea of an α cluster model, where nucleons in the nucleus are grouped into several clusters of α particles that can bond in various configurations like in a molecule. This model is different from the nuclear shell model, where each nucleon is subject to a mean-field potential obtained from all other nucleons. In the α cluster model, the interaction between two neutrons and two protons is considered first, followed by the α-α interaction (and interactions with additional nucleons).

However, for a nucleus to assume a cluster structure, it must be energetically favorable. For example, we would not expect it in ground states where the structure is usually compact, meaning that the Pauli exclusion principle becomes important due to the high degree of overlap of the clusters and so is expected to be better described by a nuclear shell model. Instead, Ikeda et al. proposed that fully clustered states have energies near the corresponding decay threshold [4]. The link between clustering and thresholds is illustrated by an Ikeda diagram in Figure 2.1, displaying α decay thresholds and possible cluster structure for the first four α-conjugate nuclei. Most nuclei have ground states far below the single α separation energy, except for ^{8}Be, whose ground state is just 92 keV above the 2α breakup threshold, suggesting a highly clustered structure. These cluster states play a crucial role in stellar nucleosynthesis, specifically α-induced stellar reactions, and hence are important to study to

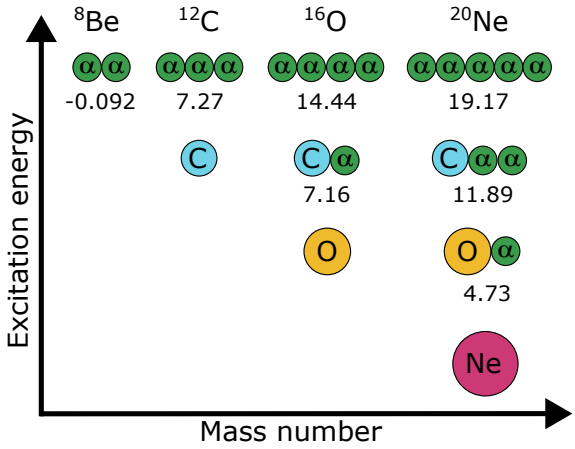

FIGURE 2.1: An Ikeda diagram [4] for nuclei with α-clustering. Clustered states are predicted to exist close to the associated decay thresholds. Energies are in MeV.

develop better stellar models and understand light element abundances in the universe.

More modern approaches are ab initio methods, which aim to describe nuclei by solving the non-relativistic many-nucleon Schrödinger equation with the realistic inter-nucleon interaction. However, the complexity of this approach arises from the theory describing this interaction, QCD, being non-perturbative in the low-energy regime relevant to nuclear physics, leading to the need for effective theories such as the chiral effective field theory to construct the Hamiltonian. For the lightest nuclei, the Schrödinger equation can be solved exactly, while various method exists to numerically find solutions for heavier nuclei such as the Green's function Monte Carlo method [5] and No-core shell model [6].

2.2 The compound nucleus

Picture an incident particle with some energy impacting a target nucleus. The projectile has a high chance of interacting with one of the target nucleons. This nucleon will then go on to make further collisions with other nucleons until the initial energy of the projectile has been distributed among the entire system of nucleons. Although the average energy of each nucleon may not be sufficient to free it from the nucleus, there is still a small chance of this occurring due to the statistical nature of energy distribution within the nucleus.

The reaction described above can be seen as a two-step process where a definite intermediate state is formed after the projectile is absorbed but before the nuclear decay occurs. This intermediate state is called the compound nucleus. The key assumption of the compound nucleus model is that the likelihood of decaying into a specific set of final products is not dependent on the means of formation of the compound. The subsequent nuclear decay will be further explained in Section 2.3.

The production probability of a compound nucleus, described by the reaction cross section, varies with the energy of the projectile. A peak in the reaction cross section at a specific projectile energy is referred to as a resonance and corresponds to a distinct state in the compound nucleus. The width of this peak is described by its decay width, Γ, which is related to the lifetime of the resonant state through $\Gamma = \hbar/\tau$ which can be seen as a manifestation of the energy-time uncertainty principle, $\Delta E \Delta t \geq \hbar/2$. The energy line profile of the cross section for a reaction $a + X \rightarrow b + Y$ is described by the Breit-Wigner distribution:

$$\sigma(E) = \frac{\pi\hbar^2}{p^2} g \frac{\Gamma_{aX}\Gamma_{bY}}{(E - E_r)^2 + \Gamma^2/4}, \tag{2.1}$$

where p is the initial momentum of the projectile in the center of mass frame, g is a statistical factor related to the spin and angular momentum of the involved particles, and E_r is the resonance energy. However, this formula only applies to isolated resonances as interference can occur with non-resonant contributions such as direct processes, elastic scattering, and tails of neighboring resonances. Moreover, broad resonances can surpass the energy separation threshold of the projectile and the target nucleus, further distorting the line shape. In these situations, the full machinery of R-matrix theory, a framework for fitting experimentally measured resonances, is used. This theory will not be further described here, but a review of the theory by Lane and Thomas can be found in [7].

2.3 Nuclear decay

In most cases, the compound nucleus will be unbound, meaning that it will decay to some final state through some decay channel. The total decay width of the state, Γ_{Tot}, will be a measure of the rate of decay. As an unbound state can decay into multiple final states, we define Γ_i as the partial decay width for

the decay to the i-th final state such that

$$\Gamma_{\text{Tot}} = \sum_i \Gamma_i. \tag{2.2}$$

Additionally, we define

$$B_i = \Gamma_i / \Gamma_{\text{Tot}} \tag{2.3}$$

as the branching ratio for the decay to the i-th final state.

In the following, two decay channels relevant to this thesis will be described. These are α and γ decays.

2.3.1 Nature of α decays

The emission of an α particle is one of the most common types of particle emission in nuclei. This is explained by the high stability and tightly bound structure of the α particle, which maximizes the released energy, Q, given by

$$Q = (m_P - m_D - m_\alpha)\, c^2, \tag{2.4}$$

where the subscripts P and D refer to the parent and daughter nucleus, respectively. Energy and momentum conservation uniquely determines the kinetic energy of the α particle in the rest frame of the parent nucleus, and in terms of the Q-value is given as

$$T_\alpha = Q \left(1 - \frac{m_\alpha}{m_\alpha + m_D} \right). \tag{2.5}$$

The spontaneous emission of an α particle is typically only possible for heavy nuclei, as the α separation threshold in light nuclei usually lies far above the ground state. Again, the only exception is ^{8}Be, whose ground state is unstable to α decay.

Fundamentally, α-decay is a quantum tunneling process. The potential experienced by an α particle with respect to its distance from the daughter nucleus is shown in Figure 2.2. Within a certain radius, a, the nuclear force prevails and the α particle experiences a spherical potential well of $-V_0$. Beyond the range of nuclear forces, i.e., $r > a$, the α particle only experiences Coulomb repulsion, given by:

$$V_c(r) = \frac{Z_\alpha Z_D e^2}{4\pi\epsilon_0 r}, \tag{2.6}$$

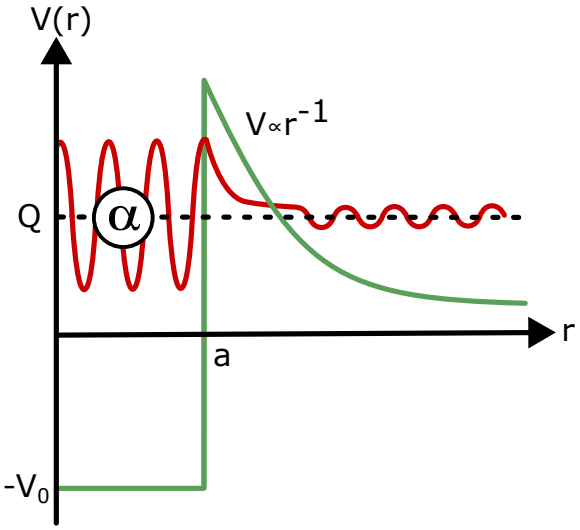

FIGURE 2.2: Potential energy (green) of a system consisting of an α particle and a daughter nucleus as a function of their separation. The α particle does not have enough energy to overcome the barrier at $V(a)$. Instead, it can tunnel through the barrier, ultimately escaping the nucleus which is manifested in the nonzero value of the wave function (red) beyond the barrier.

where Z is the atomic number. In order for the α particle, described by some wave function, to escape, it must overcome the Coulomb barrier, $V_c(a)$. However, in most cases, $Q + V_0 < V_c(a)$ and the only way for the particle to escape is through tunneling through the barrier, represented by the non-zero value of the wave function beyond the barrier. This model also shows that the probability of α decay decreases as Q decreases because there is more barrier to penetrate.

α-decay may involve transitioning from a state with one spin-parity to another, meaning that the α particle carries away angular momentum. In that case, the α particle must also tunnel through a centrifugal barrier represented by the potential $V_l(r) = l(l+1)\hbar^2/(2\mu r^2)$, where μ is the reduced mass and l is the angular momentum carried away by the α particle. This adds to the Coulomb barrier, making the barrier higher and wider for larger values of l.

Selection rules

α decay are subject to angular momentum and parity conservation laws. Conservation of angular momentum requires that the spin of the parent, $\vec{J_P}$, must be equal to the vector sum of the spin of the daughter, $\vec{J_D}$, the spin of the α

particle, $\vec{J}_\alpha$ and the orbital angular momentum in the center of mass of the daughter-α system, $\vec{L}$:

$$\vec{J}_P = \vec{J}_D + \vec{J}_\alpha + \vec{L}. \tag{2.7}$$

The α-particle has a 0^+ ground state, and hence angular momentum coupling rules dictate that the orbital angular momentum quantum number must satisfy:

$$|j_P - j_D| \leq l \leq j_P + j_D. \tag{2.8}$$

Conservation of parity requires that the product of the parity of the parent, π_P, must be equal to the parity of the daughter, π_D, the α particle, π_α, and the orbital angular momentum contribution, $(-1)^l$:

$$\pi_P = \pi_D \pi_\alpha (-1)^l. \tag{2.9}$$

Since $\pi_\alpha = +1$, a change in parity between the parent and daughter nucleus requires l to be odd, while an unchanged parity requires l to be even.

Absolute α decay forbiddance occurs in decays involving an initial and/or final state with zero spin(s). In such cases, l is limited to a single value and only a change in parity or no change in parity is possible. For decays to ground states in even-even daughter nuclei with 0^+, only decays from parent nuclei with natural spin-parity, $\pi = (-1)^l$, are allowed.

2.3.2 Nature of γ decays

A nucleus in an excited state can decay to a state with lower excitation energy by emitting a photon. Due to the relatively slow nature of γ-decays compared to particle emission, γ-emission will contribute with negligible amounts to the total decay width if some particle emission channel is open. Instead, they dominate in states below particle separation energies, or when selection rules forbid particle emission. The energy of the emitted photon corresponds to the energy difference between the initial and final states, except for a small amount that goes to the recoil of the nucleus. For light nuclei, this energy is typically only a few keV and is negligible in most cases.

γ-decay of nuclei is a result of electromagnetic changes in the nuclei. These changes can happen in two ways: either through a variation of the charge distribution in the nucleus, which results in electric radiation, or through

a change in the current distribution, which results in magnetic radiation. The radiation fields are described mathematically in terms of a multipole expansion, which is a series of terms referred to as multipole moments. The first term in the series corresponds to a photon carrying angular momentum $L = 1$ and is called dipole radiation, the second term corresponds to $L = 2$ and is called quadruple radiation, etc. For example, $E2$ represents electric quadruple radiation. Furthermore, in this framework, L is often referred to as the multipolarity, as it determines the multipole moment of the radiation field.

The transition rate, λ, of a γ ray emission from a nucleus with $E_\gamma = E_i - E_f$ depends on both the type of radiation mechanism ($\sigma = E, M$) and the multipolarity. According to Fermi's golden rule

$$\lambda(\sigma L) = \frac{1}{4\pi\epsilon_0}\frac{8\pi(L+1)}{L[(2L+1)!!]^2}\frac{1}{\hbar}\left(\frac{E_\gamma}{\hbar c}\right)^{2L+1} B_{fi}(\sigma L), \tag{2.10}$$

where $B_{fi}(\sigma L)$ is the reduced transition probability, which contains all the intrinsic nuclear information of the decay and is equal to the square of the matrix element of the multipole operator that causes the transition between the initial and final nuclear wavefunctions $\psi_i \rightarrow \psi_f$, while simultaneously creating a photon of the proper energy, parity, and multipolarity

$$B_{fi}(\sigma L) = \left[m_{fi}(\sigma L)\right]^2 = \left[\int \psi_f^* \hat{m}(\sigma L)\psi_i \, dV\right]^2. \tag{2.11}$$

Therefore, to apply Equation (2.10), the nuclear wavefunctions of the initial and final states must be known. If the electromagnetic transition is assumed to be due to a single proton transitioning from one shell-model state to another (i.e., electric radiation is due to a proton transitioning from one orbital state to a lower orbital state, while magnetic radiation is due to an intrinsic spin flip of a proton), the reduced transition probabilities can be expressed as

$$\begin{aligned} B(EL) &= \frac{e^2}{4\pi}\left[\frac{3}{L+3}\right]^2 R_0^{2L} A^{2L/3}, \\ B(ML) &= \frac{10}{\pi}\left[\frac{3}{L+3}\right]^2 R_0^{2(L-1)} A^{2(L-1)/3} \mu_n, \end{aligned} \tag{2.12}$$

where μ_n is the nuclear magneton and the nuclear radius is estimated as $R = R_0 A^{1/3}$ with $R_0 = 1.21$ fm and A is the mass number. Using Equation (2.12)

in Equation (2.10) and that $\Gamma_\gamma = \hbar\lambda$, the radiative decay widths for the four lowest multipole transitions can be written as

$$\begin{aligned}
\Gamma_\gamma(E1) &= 0.068 E_\gamma^3 A^{2/3}, & \Gamma_\gamma(M1) &= 0.021 E_\gamma^3, \\
\Gamma_\gamma(E2) &= 4.9 \times 10^{-8} E_\gamma^5 A^{4/3}, & \Gamma_\gamma(M2) &= 2.3 \times 10^{-8} E_\gamma^5 A^{2/3}, \\
\Gamma_\gamma(E3) &= 2.2 \times 10^{-14} E_\gamma^7 A^2, & \Gamma_\gamma(M3) &= 1.1 \times 10^{-14} E_\gamma^7 A^{4/3}, \\
\Gamma_\gamma(E4) &= 7.2 \times 10^{-21} E_\gamma^9 A^{8/3}, & \Gamma_\gamma(M4) &= 3.0 \times 10^{-21} E_\gamma^9 A^2,
\end{aligned} \tag{2.13}$$

with Γ_γ in eV and E_γ in MeV. The estimates in Equation (2.13) are known as Weisskopf estimates and are generally within a few orders of magnitude of the actual values. However, they should not be taken as true theoretical calculations, as transitions are often not going to be due to rearrangements of a single particle, but rather due to collective effects. Despite this, they are useful for relative comparisons with measured radiative decay widths.

Selection rules

Similar to α-decays, the conservation of angular momentum dictates that the multipolarity must satisfy

$$\left|j_i - j_f\right| \leq L \leq j_i + j_f \qquad (L \neq 0), \tag{2.14}$$

where the $L \neq 0$ ultimately can be attributed to the fact that photons are massless particles. Obviously, transitions between two states both with zero angular momentum are strictly forbidden[1]. In addition, we see that it is possible for electromagnetic transition in a nucleus to give rise to radiation that can take on one of several values of multipolarity. However, according to Equation (2.13), radiation with the lowest permitted multipolarity will dominate for reasonable values of E_γ (on the order of MeV).

The conservation of parity allows us to determine whether the radiation is electric or magnetic, based on the change in parity and multipolarity. Electric radiation has parity $(-1)^L$ and magnetic radiation has parity $(-1)^{L+1}$.

For example, the transition $2^+ \rightarrow 1^+$ has no parity change and can emit radiation with multipolarity $L = 1$, 2 or 3 and thus has three allowed electromagnetic transitions: $M1$, $E2$, and $M3$, with the $M1$ transition being dominant.

1: Instead, internal conversion can occur, where the nucleus transition to a lower-lying state by interacting electromagnetically with an orbital electron, giving it enough energy to escape the nucleus.

In general, according to the Weisskopf estimates, the emission of an electric multipole EL is approximately 10^7 times more probable than the emission of a magnetic multipole ML' for $L' = L + 1$. This number is only 10^3 comparing ML to EL' [1].

2.4 Exploring excited states with γ and β decays

As noted in the introduction, weak (β decays) and electromagnetic transitions are used to both populate and study excited states. This approach is effective because both β and γ decay have the attractive property of having their rate reliably connected to their corresponding matrix element involving initial and final states and well-known operators.

In β decays, the daughter states that are mainly populated have the same spin-parity as the parent state, with smaller contributions to daughter states with no parity change and $\Delta J = 1$. Contributions to other spin-parity daughter states are negligible and thus considered forbidden transitions. For instance, ^{12}N with spin-parity 1^+ will populate 0^+, 1^+, and 2^+ states in ^{12}C. Since ^{12}B is also a 1^+, we are limited to probing mainly 1^+ states in ^{12}C with β decay.

The spin-parity selectivity of γ decays is lower compared to β decays. This is because, in γ decay, we are not limited to only probing daughter states with a certain spin-parity. Instead, we can choose a parent state at higher energy than the daughter state, such that the daughter state of interest can be populated in favored transitions, i.e E1 and M1. For example, by selecting a 2^+ state as the parent state in ^{12}C, we can populate 1^+, 2^+, and 3^+ through $M1$ transitions, and 1^-, 2^-, and 3^- through $E1$ transitions. The challenge with using γ decays to probe the desired daughter states is that in most cases, the parent state will be unbound, leading to a high probability of particle emission, and thus the parent state must be populated at a very high rate to get a significant amount of γ decays to the daughter state.

Next, we will examine how gamma decay is identified through subsequent measurement of the emitted gamma ray with conventional gamma spectroscopy.

2.5 γ spectroscopy

γ spectroscopy is the qualitative method of measuring the distribution of energies from a γ ray source with a detector. Even though there exist various types of detectors, their basic principles of operation are the same: photons enter the detector, where they lose part or all of their energy through interactions with atoms making up the detector material. This energy releases a large number of low-energy electrons from the atoms, which are collected and transformed into an electronic signal for further processing [1]. There have been different ways in which these principles have been translated into actual functioning detectors. Undoubtedly, the two most popular types are scintillation and semiconductor detector.

2.5.1 Response function

Common for scintillation and semiconductor detectors is that they have a similar response to a monoenergetic beam, known as the response function, shown in Figure 2.3. The response function is complex due to the various ways light can interact with matter, which results in a shape that is not ideal (the ideal being a Dirac delta distribution without any associated continuum).

The photons that deposit all their energy in the detector material form a narrow peak at the expected energy in the response function and is called the photopeak. This happens through first a series of Compton scattering processes, where a photon scatters from a nearly free atomic electron, transferring parts of its energy to the electron which is then set free. At a certain point, when a photon has low enough energy ($\approx$ 100 keV), it undergoes photoelectric absorption, where it is fully absorbed by an atom resulting in one of its atomic electrons getting enough energy to escape the atom. However, if a photon wanders too close to the edge of the material and is scattered out of it before being absorbed, only a fraction of the energy is deposited, giving rise to a Compton continuum in Figure 2.3 ranging from zero to the highest energy that can be deposited, corresponding to full back-scatter, which is called the Compton edge.

Lastly, if the photon energy is greater than $2m_e c^2 = 1.022$ MeV, pair production in the material can occur where the photon creates an electron-positron pair and disappears. The positron will eventually annihilate with an atomic

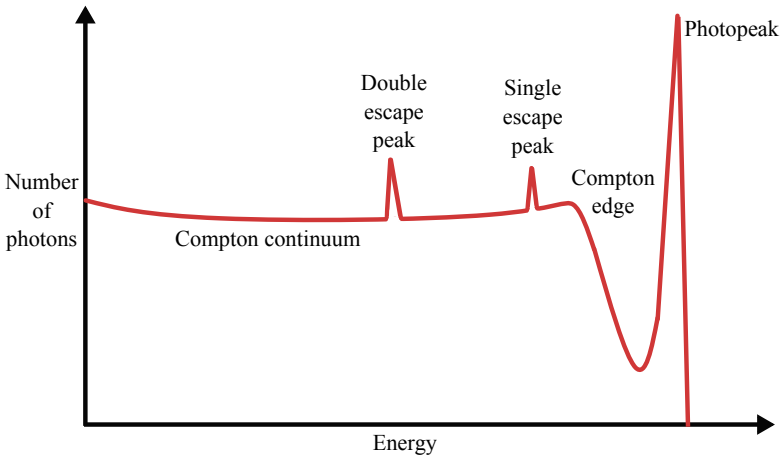

FIGURE 2.3: A typical response function of a γ detector. The photopeak represents the cases where the initial energy is fully absorbed. The Compton continuum results from the processes where the photon escapes from the detector after a few scatterings. The escape peaks result from photons escaping after a positron and an electron annihilate.

electron, resulting in two photons of energy 511 keV. These suffer one of three fates: Both are fully absorbed (ending up in the photopeak), one escapes while the other is fully absorbed, or both escape. These last two results in a single-escape peak at $E_\gamma - m_e c^2$ and a double-escape peak at $E_\gamma - 2m_e c^2$ in Figure 2.3, respectively.

The spectrum of an electromagnetic transition measured by any radiation detector will be a convolution of its inherent response function (which will be a function of the energy) and the desired energy distribution of the radiation. If the states involved in the transition have small decay widths, the energy distribution will be narrow, and the final peak in the spectrum will be in an area with low background (i.e. with a low contribution from response tails). On the other hand, if the transition involves broad states (around $\Gamma > 300$ KeV), response tails start to overlap with the low-energy part of the broad energy distribution, making it difficult to determine the real energy spectrum. In this case, a deconvolution would be necessary which is rarely feasible due to the uncertainty associated with the response functions since they may not be experimentally measured for all relevant energies. As a result, conventional direct detection of γ rays is not suitable for detecting electromagnetic transitions involving broad states, especially not if the γ branch is small as it would be lost in accumulated response tails.

As an example, consider the γ-decay from the relatively narrow 17.6 (1^+) MeV state to the 0^+ ground state and the 2_1^+ first excited state in ^{8}Be. The latter

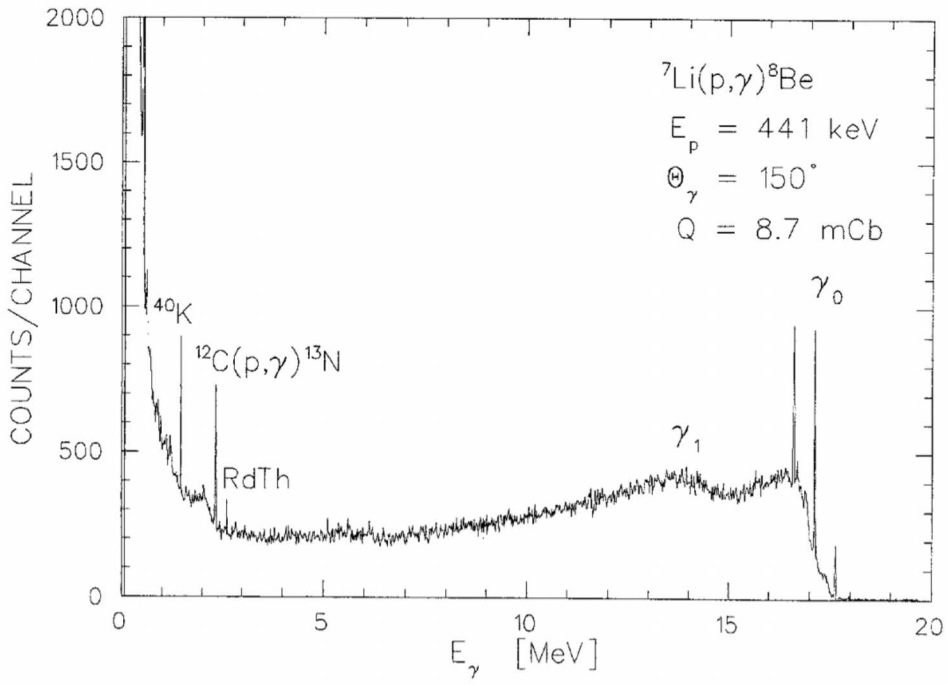

FIGURE 2.4: Measured γ spectrum from the 17.6 MeV state in ^{8}Be using a Ge(Li) detector. Figure from [8].

is a broad state at 3.0 MeV with $\Gamma = 1.5$ MeV. The γ spectrum has been recorded by Zahnow et al. in [8] using both a Ge(Li) semiconductor detector and 4π NaI scintillation detector. Figure 2.4 displays what they achieved with the Ge(Li) detector. The photopeak at 17.6 MeV from the transition to the ground state is visible as a small narrow peak. The two escape peaks are also visible and are roughly an order of magnitude larger than the photopeak. They, along with the Compton edge, completely dominate the 15-17 MeV region. Furthermore, the shape of the energy distribution of the transition to the 2_1^+ state (marked as γ_1 in Figure 2.4) is drowning in response tails from transitions to the ground state. For comparison, Figure 2.5 shows the spectrum using the NaI detector with three orders of magnitude less beam. Although the efficiency is obviously better, the resolution is significantly worse which is clear by comparing the widths of the γ_0 peak for the two detectors.

2.6 IDOG

An alternative method to detect electromagnetic transitions involving unbound states is to measure the subsequent particle breakup in coincidence instead of

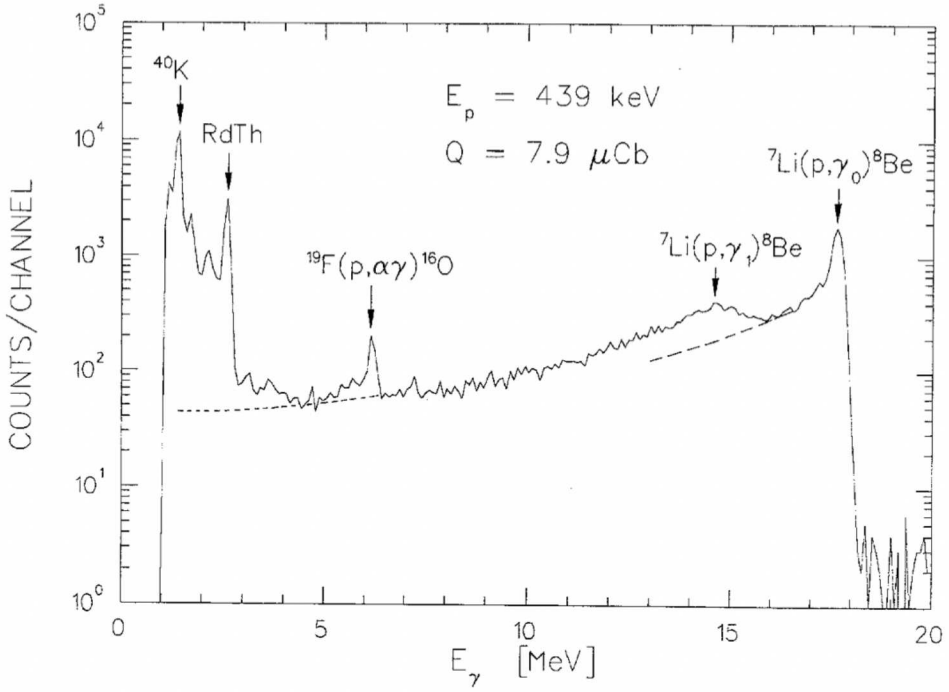

FIGURE 2.5: Measured γ spectrum from the 17.6 MeV state in ^{8}Be using a 4π NaI detector. Figure from [8].

the γ ray. In the detection of charged nuclei with semiconductor detectors, the response function will be a somewhat narrow peak if the traversing thickness of the detector is large enough for elastic nuclear collisions and inelastic Coulomb collisions to stop the nuclei completely. Accordingly, the measured particle spectrum will reliably reflect the actual spectrum of the particles. With this information, the occurrence of an electromagnetic transition can be deduced from the concept of missing energy. Taking the ^{7}Li(p,γ)$\alpha\alpha$ reaction as an example:

$$\begin{aligned} {}^7\mathrm{Li} + p &\rightarrow {}^8\mathrm{Be}(E_x) \\ &\rightarrow {}^8\mathrm{Be}(E_x') + \gamma \\ &\rightarrow 2\alpha + \gamma, \end{aligned} \tag{2.15}$$

where the initial excitation energy, E_x, is determined by the beam energy and E_x' is determined by the energy measurement of the α particles. If $E_x > E_x'$ a γ ray must have been emitted with energy $E_\gamma = E_x - E_x'$ (neglecting the recoil of ^{8}Be).

This alternative method is referred to as the method of Indirect Detection of Gamma rays (IDOG) and we can now state two key points that encapsulate the idea of the method [9]:

- Conventional γ spectroscopy is blind towards even moderately broad states.
- The IDOG method is essentially background-free and the sensitivity of the method is independent of the width of the resonance.

The latter is associated with measuring the particle breakup in multi-particle coincidences and the simple response function of charged particles in semiconductor detectors.

The IDOG method was first explored by Alcorta et al. and Kirsebom et al. in 2009 [10, 11]. They demonstrated the technique using the γ-delayed 3α breakup of ^{12}C and were able to identify γ decays from the narrow 15.11 and 12.71 MeV states to broad states above the breakup threshold with an efficiency comparable to standard γ-spectroscopy but in an essentially background-free environment. Since the method was first suggested, it has been successfully used to study the γ-delayed 3α breakup of the 17.76 and 18.85 MeV states in ^{12}C by Kirsebom et al. and the γ-delayed 2α breakup of the 17.64 MeV state in ^{8}Be by Munch et al. [12, 13].

Using the IDOG method, Munch et al. were able to reconstruct the full ^{8}Be excitation spectrum populated in the γ decay of the 17.6 MeV state. That spectrum is shown in Figure 2.6. The γ-decay to the 2^+_1 state is easily seen at 3 MeV in an almost background-free environment. Furthermore, the practical dynamic range is very large, and we are even able to observe the small γ branches to the 16.6 and 16.9 MeV states, which correspond to γ energies of 0.7 and 1 MeV, respectively. These would not be measurable using conventional detectors due to room background and response tails, as shown in Figure 2.4 and Figure 2.5.

The success of the IDOG method relies on the feasibility of measuring the multi-particle breakup in complete kinematics, i.e. being able to obtain complete and accurate energy and momentum information of all the involved particles. This has become possible with the advancements in silicon strip detectors and electronics over the last few decades [10]. This complete information allows for the almost complete removal of noise and random coincidence events with relatively simple analytical techniques.

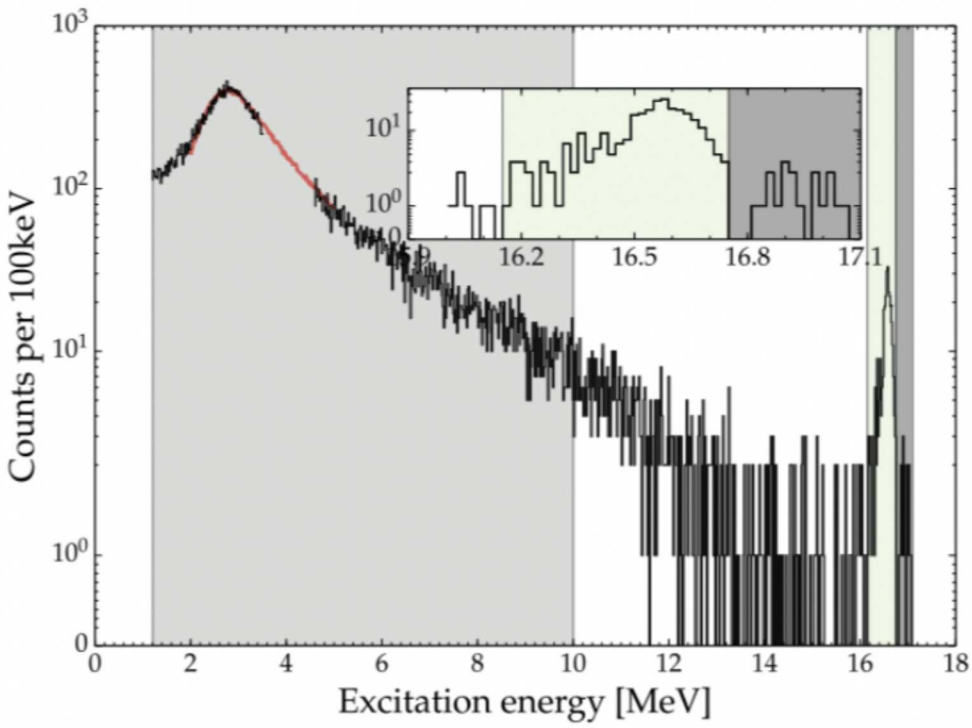

FIGURE 2.6: The excitation spectrum of ^{8}Be, as obtained using the IDOG method on a γ-delayed 2α breakup experiment, is shown. The insert provides a close-up of the region with the two states at 16.6-16.9 MeV. Figure from [13].

Chapter 3

γ decay in ^{16}O

3.1 Motivation

The evolution of baryonic matter in the universe is heavily influenced by the ^{16}O compound nucleus. It plays a major role in key stellar burning phases and nucleosynthesis processes in stars, for instance, in stellar hydrogen burning in massive main sequence stars, the level structure of the ^{16}O compound nucleus determines the branching of ^{15}N(p,α)^{12}C vs. ^{15}N(p,γ)^{16}O in the CNO cycle.

The subsequent helium-burning phase is characterized by the possibility of 3α processes to occur in the stellar core, where three α particles fuse into a ^{12}C nucleus, releasing 7.5 MeV. It ignites when the hydrogen in the stellar core is depleted, leading to a gravitational contraction of the core, increasing the temperature and density of the core matter. A subsequent capture of an α particle can form ^{16}O through ^{12}C(α,γ)^{16}O which releases 7.2 MeV. This reaction, along with the 3α process, largely defines the ^{12}C/^{16}O ratio in hydrostatic helium burning, which in turn influences the subsequent stellar evolution, and ultimately defines the abundances of carbon and oxygen in the universe that are crucial for biological life [14]. Hence, much effort has been invested in determining the astrophysical reaction rate of these processes in the past 70 years.

The simultaneous fusion of three α particles to create the 3α process is considered unlikely. Instead, a more efficient two-step process is considered more probable, in which two α particles first fuse to form ^{8}Be. The capture of a third α particle is hindered by the ground state of ^{8}Be being unbound,

resulting in a small cross section for the second capture. However, owing to the existence of the Hoyle state, a highly α clustered resonant state in ^{12}C discovered by Hoyle in 1954 [15], the cross section of the second capture is greatly enhanced and the formed ^{12}C can become stable by a subsequent γ decay. The 3α reaction rate mainly depends on the strength of the Hoyle state, with higher-lying resonances only playing a significant role at higher stellar temperatures. The current estimate for the uncertainty in the 3α reaction is around 10% at relevant astrophysical energies [14].

Determining the ^{12}C(α,γ)^{16}O reaction rate is not as straightforward due to a much more complex reaction mechanism. The reaction does not proceed through a single narrow resonance, but instead, the cross section is characterized by complex interference between overlapping resonances and nonresonant reaction components. The strength of these components is directly connected to the nuclear structure of the ^{16}O compound nucleus, which is shown schematically in Figure 3.1. Being an even-even nucleus, it has a 0^+ ground state. It has four particle bound states at $E_x = 6.05$, 6.13, 6.92, and 7.12 MeV with 0^+, 3^-, 2^+, and 1^-, respectively, where the two odd parity states can be considered to be single-particle configuration well described by a shell model while the two even parity states are better described by a cluster model [14]. The α separation energy is only a few hundred keV above both the 2^+ and 1^- bound states. α decay selection rules allow only natural parity states in the ^{16}O compound nucleus to be populated and thus γ decay selection rules allow only electric transitions to the 0^+ ground state.

At the center of mass energies relevant for hydrostatic helium burning $E_{\mathrm{CM}} \approx 0.3$ MeV, the ^{12}C(α,γ)^{16}O reaction rate is dominated by E1 and E2 resonant capture to the ground state. The E1 component stems from the interference between the tail of the subthreshold 1^- state and the unbound 1^- state at 9.59 MeV. Similarly, the E2 component stems from the interference between the tail of the subthreshold 2^+ state and the unbound 2^+ state at 9.84 MeV. Typically, E1 transitions are stronger than E2 transitions ($\Gamma(E2)/\Gamma(E1) \approx 10^{-5}$). However, a specific isospin, T, selection rule applies, forbidding $\Delta T = 0$ E1 transitions in self-conjugate nuclei (nuclei with an equal number of protons and neutrons)[18]. Both the 1^- states and the ground state have $T = 0$. Despite this, the transitions occur but at reduced strength, as Coulomb interactions between protons break isospin symmetry, making the states isospin mixed. As a result, the E1 and E2 components are nearly equally strong. Additionally,

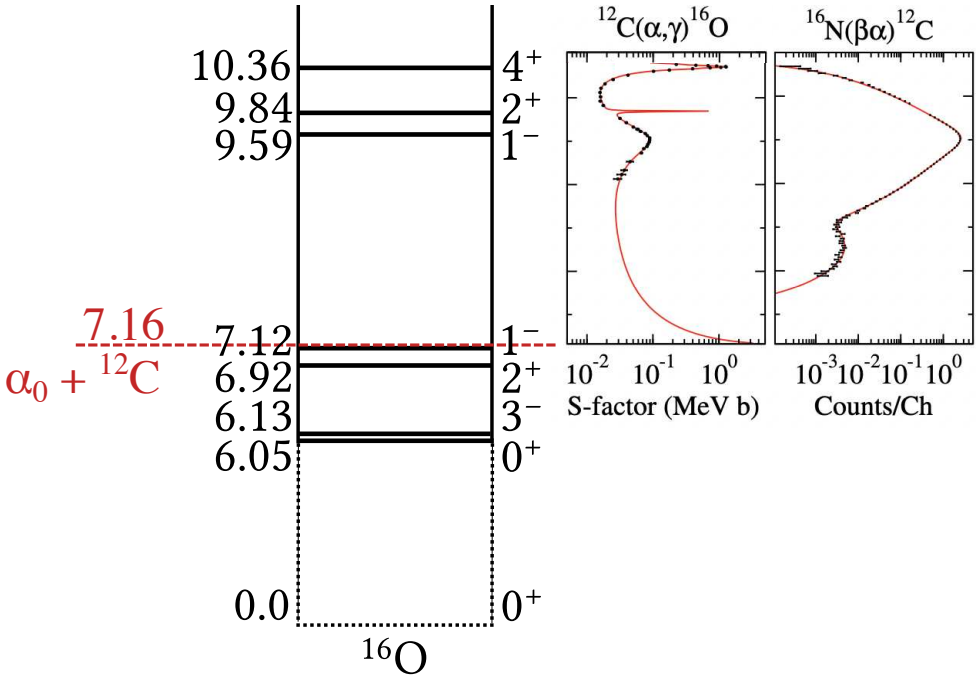

FIGURE 3.1: The level structure of the ^{16}O compound nucleus with energies in MeV. Unnatural parity states are omitted. The red dotted line marks the α separation energy to the ground state of ^{12}C. Data from ^{12}C(α,γ)^{16}O and ^{16}N($\beta\alpha$)^{12}C experiments is shown to the right, with the energy axes converted into excitation energies and aligned with the level diagram. The former data show the S-factor of the reaction and is from Schürmann et al. [16], while the latter shows the α spectrum and is from Buchmann et al. [17]. The solid red lines are phenomenological R-matrix fits from deBoer et al. [14], where the two figures are also from.

it is worth mentioning that there are small contributions to the reaction rate from cascade transitions where γ decay does not occur directly to the ground state.

At $E_{CM} = 0.3$ MeV, the Coulomb repulsion between the two charged particles makes the cross section over the Gamow window $\approx 10^{-17}$ b. To be able to measure this, it would require a five-order of magnitude improvement in current state-of-the-art detector sensitivity [19]. Therefore, the best we can do is extrapolating the cross section to the relevant low-energy region. The first graph in Figure 3.1 shows data of the ^{12}C(α,γ)^{16}O cross section in the form of an S-factor, where the extrapolation to lower energy was performed using phenomenological R-matrix theory. The S-factor expresses the astrophysical reaction cross section without the trivial energy dependencies (e.g. Coulomb repulsion).

A precise and accurate extrapolation requires the inclusion of complementary data obtained with indirect methods. One such method is the β-delayed α decay of ^{16}N, which can constrain the extrapolation of the E1 component. This reaction only provides information about the E1 component because the β decay of ^{16}N (2^-) to 1^- states in ^{16}O are allowed transitions, while the decay to 2^+ states are forbidden transitions. The second graph in Figure 3.1 shows the α spectrum from an ^{16}N($\beta\alpha$)^{12}C experiment. The unbound 1^+ state is clearly visible, and the low-energy interference anomaly accompanying the main α peak is due to the tail of the subthreshold 1^- state, also known as a ghost contribution.

An alternative method to populate the unbound 2^+ and 1^- state is through γ decay from higher-lying excited states. Good candidates are a $2^-, T = 1$ and $1^-, T = 1$ state at 12.97 and 13.09 MeV, respectively, which can populate the states of interest through $E1$ or $M1$ transitions. The proton separation energy in ^{16}O is 12.13 MeV, thus these parent states can be populated by firing protons on ^{15}N.

To determine the feasibility of this alternative method, the work presented here will apply the IDOG method to ^{15}N(p,α)^{12}C data to see if the γ-delayed α decay from the 12.97 and 13.09 MeV states to the 9.59 and 9.84 MeV states can be detected and in that case, determine radiative decay widths of these transitions which there exist no experimental values of in the literature. Additionally, the study will also look for any other transitions to natural parity states above the α separation energy.

3.2 The γ-delayed α decay of ^{16}O

The γ-delayed α decay is schematically shown in Figure 3.2. The parent states are populated in the $p + {}^{15}\mathrm{N} \rightarrow {}^{16}\mathrm{O}^*$ reaction. The states of interest are then populated through a γ decay and will subsequently α decay to the ground state of ^{12}C, in which case we denote the emitted particle as α_0. However, since the populated parent states are unbound, they will mostly α decay directly to the ground state in ^{12}C or to its first excited state (α_1). The exception is the unnatural parity parent state, 2^-, which is forbidden from decaying to the ground state in ^{12}C by selection rules.

There are seven natural parity states between the parent states and the states of interest. These states, along with the two states of interest, are listed

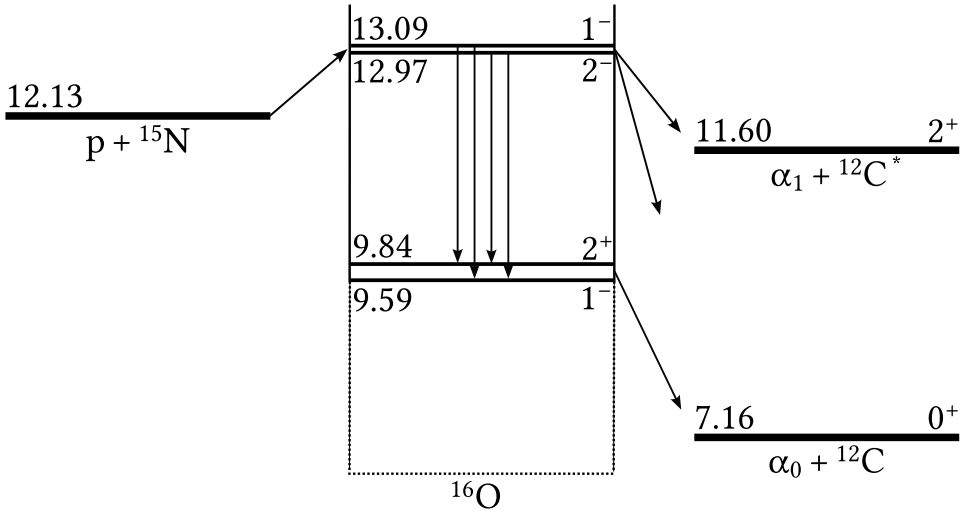

FIGURE 3.2: The level structure of the ^{16}O compound nucleus. Unnatural parity states are omitted.

TABLE 3.1: Excitation energy, spin-parity, and isospin, and the total decay width for all natural parity states above the α separation energy that can be populated through γ decay from the 12.97 and 13.09 MeV states. The values are taken from [20].

E_x [MeV]	J^π, T	Γ_{Tot} [keV]
12.44	$1^-, 0$	91
12.05	$0^+, 0$	1.5
11.60	$3^-, 0$	800
11.52	$2^+, 0$	71
11.26[1]	$0^+, 0$	2500
11.10	$4^+, 0$	0.28
10.36	$4^+, 0$	26
9.84	$2^+, 0$	0.625
9.59	$1^-, 0$	420

in Table 3.1 with their spin-parity and total decay width. These are all the states through which the γ-delayed α decay from the two parent states could occur.

The radiative decay widths of the two parent states to the states in Table 3.1 are expected to be much smaller than the particle emission decay widths. Weisskopf estimates for these transitions, for the lowest allowed multipole, are given in Table 3.2.

1: The existence of this level seems uncertain in the literature, but was included anyway for completeness.

TABLE 3.2: Weisskopf estimates of the γ decay from the 12.97 and 13.09 MeV states to natural parity states above the α separation energy.

Initial state (MeV, J^π)	Final state (MeV, J^π)	Lowest-multipole allowed transition	Γ_γ (eV)
12.97, 2^-	12.44, 1^-	M1	3.1×10^{-3}
	12.05, 0^+	M2	9.6×10^{-8}
	11.60, 3^-	M1	5.3×10^{-3}
	11.52, 2^+	E1	1.3
	11.26, 0^+	M2	2.1×10^{-6}
	11.10, 4^+	M2	3.4×10^{-6}
	10.36, 4^+	M2	1.8×10^{-5}
	9.84, 2^+	E1	13
	9.59, 1^-	M1	0.81
13.09, 1^-	12.44, 1^-	M1	5.3×10^{-3}
	12.05, 0^+	E1	0.48
	11.60, 3^-	E2	1.5×10^{-5}
	11.52, 2^+	E1	1.7
	11.26, 0^+	E1	2.6
	11.10, 4^+	E3	7.0×10^{-10}
	10.36, 4^+	E3	6.4×10^{-9}
	9.84, 2^+	E1	15
	9.59, 1^-	M1	0.90

To be resonant on the 12.97 and 13.09 MeV states, the proton beam energy should be 896 and 1024 keV, respectively. Two moderately broad nearby natural parity states at 13.02 (2^+) and 13.12 (3^-) MeV will inevitably also be populated. However, they are both $T = 0$ states, and thus the $E1$ and $M1$ transitions from these nearby states to the states of interest are forbidden or at least appreciably weaker than average.

3.3 Experimental methods

Two ^{15}N(p,α)^{12}C experiments were carried out in May 2022 at the Department of Physics and Astronomy at Aarhus University. The experiments were done with proton energies of 902 keV for 1h46min and 1028 keV for 1h52min and referred to as the 902 and 1028 keV experiment, respectively. This section outlines the experimental setup that was used and describes the process from raw data to analyzed data. First, an overview of the accelerator facility is

presented, followed by a description of the detectors and data acquisition system. Finally, the software used is introduced.

3.3.1 The 5 MV Accelerator facility at Aarhus University

The $^{15}N(p,\alpha)^{12}C$ reaction was carried out at the 5 MV Van der Graaf accelerator at the Department of Physics and Astronomy at Aarhus University. The accelerator works by accelerating charged particles through a static electric potential created by a moving conveyor belt. Although the name suggests a maximum voltage of 5 MV, in practice, the usable voltages are lower, typically in the range of 1 to 3 MV and not exceeding 4 MV.

A schematic of the facility is shown in Figure Figure 3.3. The conveyor belt establishes a continuous transfer of positive static charges by rubbing against a comb-shaped electrode connected to a positive DC voltage supply, stripping off electrons from the belt and leaving it positively charged. The other end of the belt is electrically connected to a conducting dome, which spreads the charge and creates a strong electromagnetic field outside the dome, used to accelerate charged particles through the Lorentz force.

Inside the dome, gas is ionized into plasma through an ion source using an RF-field to strip away electrons. Commonly used ions at the facility include H^+, H_2^+, $^3He^+$, and $^4He^+$. A weak extraction potential moves the plasma into an acceleration tube, where the plasma is accelerated and focused into a beam of charged particles due to the positive charges on the dome.

The strong electric buildup on the dome causes sparks to the surrounding area. To prevent this, the accelerator is enclosed in a pressurized vessel filled with sulfur hexafluoride (SF_6), which has excellent insulating properties for a Van de Graaf accelerator. Due to international regulations on sulfur hexafluoride, which is a very potent greenhouse gas, a 4:1 mixture of N_2 and CO_2 is sometimes used instead, even though its breakdown potential is lower than sulfur hexafluoride [21].

The beam passes through deflection plates, a quadrupole, two sets of slits, a beam scanner, and a Faraday cup for stability and focus before encountering a dipole electromagnet for precise mass-to-charge ratio selection to ensure a beam of the desired ions. Before reaching the reaction chamber the beam passes through a series of slits to make the final adjustments.

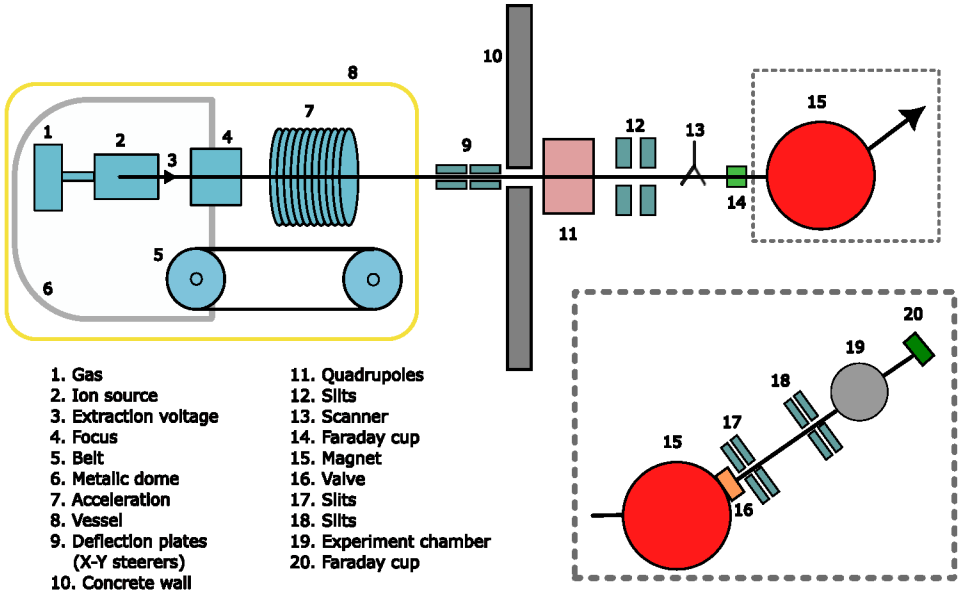

FIGURE 3.3: A schematic of the 5MV Van de Graaf accelerator at Aarhus University. After passing the magnet, the beam can be directed through several beam lines and used for various types of experiments. The components within the gray dotted lines, labeled 16 to 20, represent the subatomic beam line. The figure is largely inspired by a similar figure by Oliver Kirsebom.

The reaction chamber is where the nuclear reactions of interest occur and are detected with the detector setup. The details will be covered in the next section. After the reaction chamber, there is a Faraday cup that measures the number of ions hitting it based on the induced current in the metal cup. The cup is positioned 1m downstream along the beam line from the chamber to minimize the amount of backs-scattered beam into the reaction chamber.

3.3.2 Detector Setup

A total of four Double-sided Silicon Strip Detectors (DSSD) from *Micron Semiconductor Ltd* [22] were used in the experiment, two of which were quadratic (model W1) and two annular (model S3). The DSSD is a semiconductor detector that measures the energy of traversing ionizing particles by counting the number of charge carriers (electron-hole pairs) set free in the material between two electrodes. By applying a bias voltage, the electrons and holes move to the electrodes, creating an electrical signal proportional to the energy of the incident particle. The two electrode-connected regions are doped (one

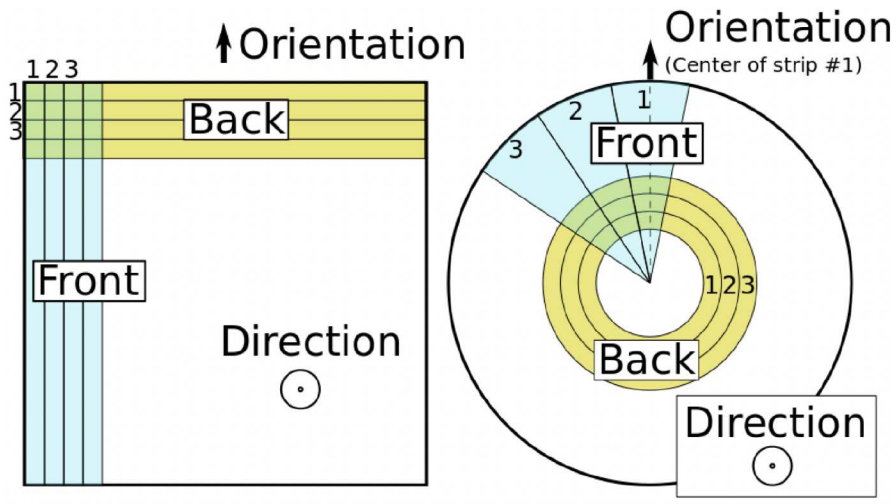

FIGURE 3.4: The DSSD used in the experiment is illustrated, showing the arrangement of the strips. On the left side is the W1 model, which has 16 front and back strips. On the right side is the S3 model, which has 32 spokes on the front and 24 rings on the back.

p-doped, one n-doped) to prevent leakage current and accurately measure the particles' energy [23].

Both models used in the experiment have each side of the detector divided into strips, with the back strips orthogonal to the front strips, effectively forming a grid of pixels at each strip intersection. This allows for both the energy and position of the incident particle to be measured, which is essential for complete kinematics studies. This is shown schematically in Figure 3.4 for both models.

The W1 model has an active area of 50x50mm^2, divided into 16 rectangular strips on each side, resulting in a total of 256 pixels. Each pixel has an area of 3x3mm^2, with an inter-strip width of 0.1mm made of aluminum. The active area has a thickness of 60μm and includes a 100nm p-doped layer implanted in the front and covered by a thin aluminum contact grid, as well as a 400nm n-doped layer implanted in the back and covered by a thick aluminum layer. The doped layers act as dead layers, where energy from ionizing particles can be deposited without contributing to the final electrical signal. The thin front dead layer minimizes energy loss in the inactive region, while the back dead layer is not a concern since the incident particles should be fully stopped in the material.

The S3 model has a radius of 35mm with a central hole of 11mm. The front is divided into 32 radial spokes, while the back has 24 rings, creating a total

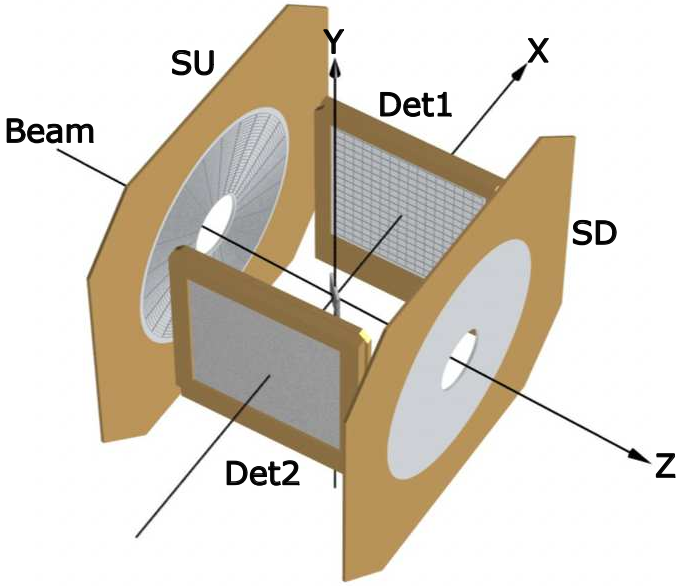

FIGURE 3.5: Illustration showing the detector setup.

of 768 pixels of various sizes ranging from 2.26mm^2 in the innermost ring to 6.77mm^2 in the outermost ring. The total thickness is 1000μm, with a total dead layer of 507nm on the front and 4μm on the back.

In nuclear reaction experiments, it is often desired to measure particles in coincidence, which requires a large solid angle coverage of the detector setup. This is achieved at the Van de Graff accelerator at Aarhus University, as shown in Figure 3.5. The two S3 detectors are positioned such that the beam passes through their center holes. The one downstream from the beam is labeled SD, while the upstream one is referred to as SU. Additionally, the two W1 detectors, positioned on the left and right of the beam, are called Det1 and Det2, respectively. The solid angle coverage is roughly 38% of 4π.

In the center of the detector setup is the target, which is mounted on a vertical metal ladder. The target consisted of a 40nm layer of C_2N on a 4μg/cm^2 carbon backing. To prevent particles that would otherwise hit the W1 detectors from hitting the frame of the metal ladder, the ladder had to be positioned at a 45 degree angle relative to the beam.

3.3.3 Data Acquisition System

The conversion of an electrical signal generated when an incident particle deposits its energy in one of the detectors into digital numeric values is ac-

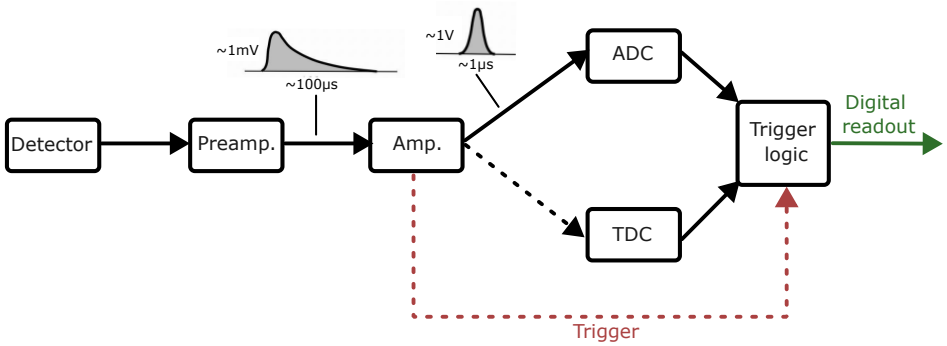

FIGURE 3.6: Flow diagram of the signal processing chain of the DAQ. The dotted lines represent logic signals. The figure is inspired by a similar figure by Erik Asbjørn Mikkelsen Jensen.

complished by the data acquisition system (DAQ). The signal processing chain of the DAQ is depicted in Figure 3.6.

The electrical signal from the detector is first amplified by a preamplifier to a suitable level for further processing. This is done by integrating the current over a capacitor, resulting in a fast-rising linear pulse with a long tail of $\approx 100\mu$s. The pulse height of the output signal will be the variable carrying the information about the energy of the incident particle.

The signal is then sent to an amplifier for further shaping and amplification, producing a Gaussian-shaped signal with a width of $\approx 1\mu$s which is referred to as the energy signal. Before it is sent to the Analog-to-Digital Converter (ADC), it passes through a discriminator to eliminate noise by checking if the amplitude is above a certain threshold. The amplifier also produces two logic signals: a time signal that is sent to the Time-to-Digital Converter (TDC) with a delay, and a signal sent to the trigger component of the DAQ for logical operations.

To trigger data acquisition, the trigger component imposes conditions such as a lower trigger threshold, a Det1-Det2 and SD-SU coincidence trigger condition, and a requirement to only acquire data every 8th trigger in the SD. If all inputs to the trigger system result in a 'TRUE' outcome, a logic trigger signal is sent to the ADC and TDC, allowing data to be collected for the following 3μs. During this time, the ADC determines the pulse height and the TDC determines the relative time of arrival of the detected particles. All the data collected in this time window constitutes an event.

After the time window closes, the data from the ADC and TDC are converted into digital form and read out, which takes a few microseconds. During this time period, no signals can be processed and is referred to as the dead time of the DAQ.

3.3.4 Root and AUSAlib

The digital readout from the acquisition system is stored to disk in a binary format, so it must be transformed into a form suited for subsequent analysis. Since this is common for many types of experiments, a set of powerful tools and routines have been developed, which will be explained here.

The data is processed through an object-oriented C++ framework called ROOT [24], which was created at CERN in 1994 to replace the then-used FORTRAN library, which was struggling to handle the large amounts of data produced in particle and nuclear physics experiments. Thus, one of the main features of ROOT is its efficiency in handling large quantities of data, especially in experiments with many events that have the same data structure, as it allows for selective access to these events, which are assumed to be independent. The storage class that is used for this purpose is called the TTree, consisting of branches referred to as TBranch, each corresponding to a variable of the event, such as the energy deposited in the front of one of the detectors.

The transformation of raw data into analyzable data is a task common in most nuclear experiments and a common framework was developed at the subatomic group at Aarhus University, called AUSAlib (Aarhus University SubAtomic library)[25]. AUSAlib can be considered an extension of the ROOT framework, and it consists of several individual modules that each handle a distinct step in the transformation process. A simplified pipeline of the process is shown in Figure 3.7. The figure also includes an extension to AUSAlib, called simX, which is a Monte Carlo simulation library.

In the upcoming sections, the individual modules in AUSAlib will be outlined. The practical application of these components in the study presented here will be presented in Section 3.4.

Unpacker

The experimental data goes through an unpacker module first. The unpacker converts the raw data from the digital readout into the ROOT TTree format

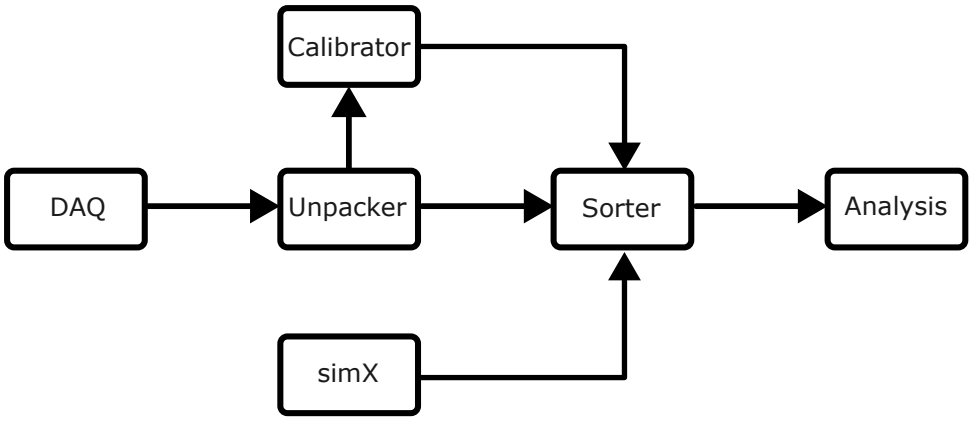

FIGURE 3.7: Flow diagram of the AUSAlib pipeline.

using the third-party program ucesb [26]. The output is referred to as the unpacked file. In this file, each event has its own set of TBranches stored in the TTree. Four branches exist for each of the four detectors (DET1, DET2, SU, SD) back and front (B, F). These branches are the (1) multiplicity, (2) identity (strip numbers hit), (3) ADC values, and (4) TDC values.

As an example, consider the following branches for an event:

$$\begin{aligned} \text{DET1F} &= 2 \\ \text{DET1FI} &= [3, 5] \\ \text{DET1F\_E} &= [525, 725] \\ \text{DET1F\_T} &= [250, 600] \\ \text{DET1B} &= 2 \\ \text{DET1BI} &= [3, 5] \\ \text{DET1B\_E} &= [500, 700] \\ \text{DET1B\_T} &= [260, 610]. \end{aligned} \tag{3.1}$$

In this example, DET1 was hit twice (multiplicity of two). The third front strip was hit with ADC and TDC values of 525 and 250, respectively, and the fifth strip was hit with 725 and 600. Similarly for the back of DET1. In the unpacked files, the ADC value is a value between 0 and 4096 (12-bit) and is called the channel number. The TDC value is in units of 10^{-10}s.

Calibrator

For each strip, an appropriate energy calibration is required to transform the channel numbers into energies. This is done with the calibrator tool. Assuming a linear correlation between channel number and energy, this correlation is determined by comparing the measured spectrum of a known source (typically a radioactive source emitting α particles with known energies) with the expected spectrum.

The peak locations are then identified using a peak-finding algorithm, and a multi-Gaussian fit is performed to obtain the final peak location estimates. This results in a set of [channel, energy] values that are linearly fitted to obtain the two calibration coefficients. The output of the calibrator is a two-column file containing these coefficients for each strip of the detector.

The calibrator also accounts for the energy loss in the detector's aluminum dead layer. This loss is described by the stopping power of the material (dE/dx), which is the amount of energy lost per unit length. The energy loss is calculated by multiplying the stopping power by the effective thickness of the material, which depends on the angle of incidence, θ,

$$\Delta E = \frac{dE}{dx}\frac{\Delta x}{cos\theta}, \tag{3.2}$$

where Δx is the actual thickness of the material. The stopping power is calculated using SRIM [27].

Sorter

The purpose of the sorter is to perform the energy calibration and matching on the unpacked file. It requires a JSON file that includes information about the detectors such as position, orientation, and individual calibration files.

The matching process involves combining events from the front and back sides of the detector. When there is only one hit, it is straightforward. But, with multiple hits (especially due to noise), the algorithm sequentially picks front-back pairs with the lowest energy difference. In Figure 3.8 this matching principle is illustrated using the same example as in Equation (3.1) (assuming a 1:1 energy calibration). The example shows the most probable combination of front-back matching among the two possibilities.

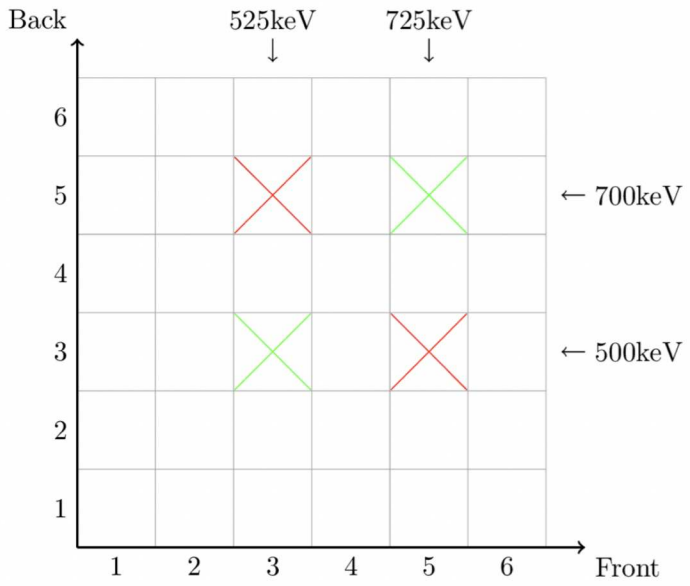

FIGURE 3.8: A 6x6 grid representing the intersection of six front and back strips in a detector. The detector has detected two particles with energies of 525 keV and 725 keV at the front and 500 keV and 700 keV at the back. Two matching combinations are possible, but the one with the pairs having the smallest energy difference is the most probable and are thus matched. This match is highlighted in green.

The sorter also takes a second JSON file, called the matcher file, as input. This file allows the user to specify matching constraints such as an upper energy tolerance and a lower cut on the matched energy, which are great tools to reduce noise. Additionally, it enables the user to disable individual strips by omitting their data from the sorted file, which can be useful if detectors have malfunctioning strips.

After matching, the hits from the front and back sides of each detector are merged into a single hit. Thus the hit can now be considered as consisting of actual *particle* hits, making it possible to associate physical properties with each particle, such as its polar angle. The sorted file contains the following branches: front and back strip hit (FI, BI), energy (FE, BE), and time (FT, BT), multiplicity (mul), polar angle (theta), azimuthal angle (phi), and detector number (id). By doing so, the number of branches has been reduced from 32 in the unpacked file to 10 in the sorted file.

simX

simX is a powerful tool capable of performing Monte Carlo simulations of the kinematics of nuclear reactions or decays. In particular, it is very useful

for determining detection efficiencies and optimizing detector setups prior to experiments. The simulated data is stored in the same format as experimental data (i.e. as an unpacked file) and can go through the same sorting and analysis process. Dummy calibration files must be provided to simX to counteract any calibrations so that the correct energy values are obtained when the actual calibration is performed.

The simX requires four input files. The user needs to give files providing all the information related to (1) the detectors, including type, position, thickness, and trigger conditions, (2) the beam, including energy, origin, beam direction, and the spread on all these values, (3) the target, including position, orientation, thickness and material, and (4) the reaction. The latter is called the reaction file and states the beam and target nuclei in the reaction. The user must also specify the decay chain to the final decay product that will be detected, including the excitation energy of the nuclei, and optionally the width and weight, which is the line shape of the state, such as a Breit-Wigner shape.

It is worth noticing that simX does not yet have the capability to simulate nuclear reactions temporally. As a result, the FT and BT branches will not be present in the sorted files of simulated data.

3.4 Data Reduction

In this section, I will present the calibration and sorting process of the 902 and 1028 keV experiments. The subsequent analysis to calculate relevant variables and identify true coincidences is also presented.

3.4.1 Calibration and sorting

A triple α source consisting of the isotopes ^{148}Gd, ^{239}Pu and ^{244}Cm were used for calibration. They emit α particles at one, three, and two energies, respectively, and these are listed in Table 3.3. The source was positioned facing a detector and data was collected for up to 19 hours to optimize the calibration. An alpha spectrum, with the peak-finding and multi-Gaussian fitting routine applied, is shown in Figure 3.9. The three main peaks are clearly seen and the algorithm is also able to identify the sub-peaks. A plot of the residuals for all six peaks is also shown in the same figure. The systematic behavior of the residuals across all strips and detectors suggests that the isotopes were implemented in layers,

TABLE 3.3: α energies of the triple α calibration source. Values from [28].

Isotope	E_α [keV]
^{148}Gd	3182.69
^{239}Pu	5105.5
	5144.3
	5156.59
^{244}Cm	5762.64
	5804.96

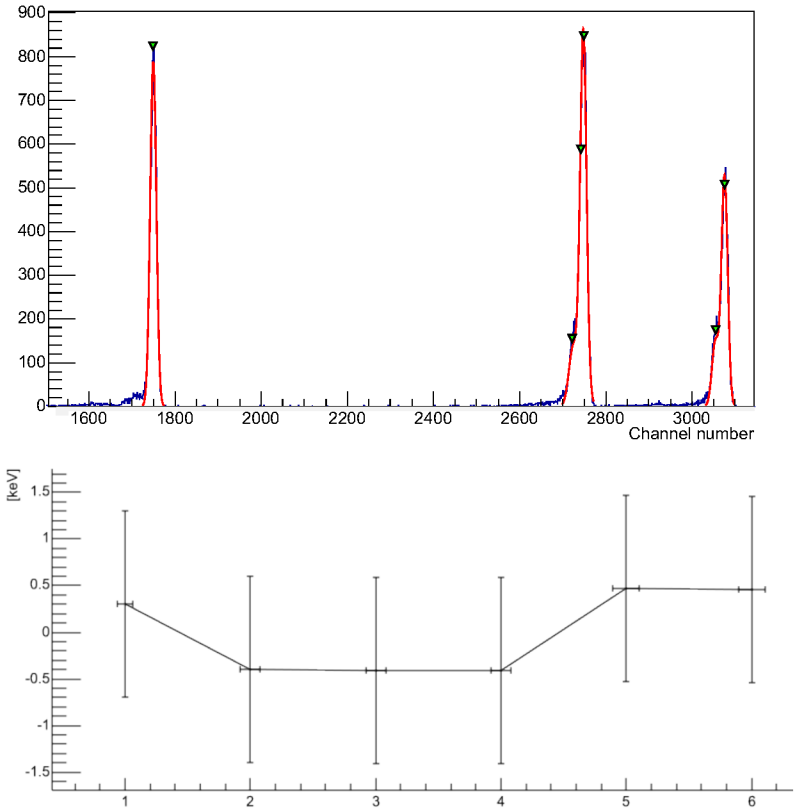

FIGURE 3.9: (Top) The α spectrum measured by the 14th back strip on Det1. The red curves are the multi-Gaussian fit with the green arrows showing the positions of the peaks. (Bottom) The residuals of final fit, where the abscissa indicates the peak as they are listed in Table 3.3.

with ^{239}Pu at the bottom, leading to alpha particles losing energy in the two front layers. Despite this, the residuals are still relatively small compared to the detector resolution.

In both experiments, the data from the SD and SU detectors were omitted due to hardware issues with only 14 out of 24 rings functioning properly in

the SD and an excessive amount of Rutherford scattering. This was realized by observing hit patterns in the sorted files. As a result, only Det1 and Det2 were used, reducing the detector solid angle coverage to 27%.

An initial front-back matching tolerance of 100 keV and a lower cut of 100 keV on Det1 and Det2 were applied. However, many coincidences were discarded because many hits in Det2 did not meet the front-back matching threshold. The problem was found to be caused by incorrect calibration of the front strips in Det2, leading to a large front-back energy difference. This issue was resolved by increasing the matching tolerance to 1 MeV and using only the energy deposited in the back strip for further analysis.

3.4.2 Analysis

The final step in the data analysis process is to analyze the sorted file and combine the detector hits into physical events. An analysis program was developed that took the sorted, target, and setup files as input and calculates the physical properties of the detected particles. The results are saved in TBranches of a new ROOT file. The overall functioning of the analysis can be broken down into four steps:

1. *Hit finding*: For all detected events, a loop over the multiplicity is performed, in which all information about a single hit in the event is stored within its own 'Hit' object. This information is deposited energy, hit position, polar angle, etc.

2. *Hit parring*: For events with a multiplicity of two or higher, steps 3. and 4. are repeated for every combinatory hit pair within the event. Only pairs that were detected with a time difference of less than 100ns are considered since we would not expect true α-^{12}C coincidences to be detected with a time difference larger than that.

3. *Energy correction*: The α particle is expected to have the largest energy due to the mass difference, so the hit with the largest deposited energy is assumed to be the α. The energy of both particles is then corrected for energy losses in the target and detector dead layer, using the setup and target geometry information from the setup and target file.

4. *Variable calculations*: The final step is to calculate the desired variables of the physical event. From the mass, energy, and direction, the four-momentum of each particle is constructed and boosted to the center of mass. The energy in the CM is then extracted and the excitation energy in the ^{16}O compound nucleus can be calculated using the invariant mass method

$$E_{\mathrm{x}} = (p_\alpha + p_C)^2 - m_O, \tag{3.3}$$

where p is the four-momentum. Each calculated value is saved to its own branch in the new ROOT file, such that a single branch contains all values of a certain variable for all analyzed events.

3.4.3 Coincidence reduction

In Figure 3.10, the center of mass energies of the emitted particle and its recoil are displayed for the 902 keV experiment. Although we are tempted to refer to the emitted particle as the α particle and the recoil as ^{12}C, we are cautious since a significant portion of the data will be false coincidences. These appear due to background noise and Rutherford scattering of protons on ^{15}N and ^{12}C. They can be reduced by imposing kinematic constraints on the data that we know true α-^{12}C coincidences should fulfill. These constraints will be called cuts. In total, three cuts will be imposed on the data, and they will be presented in the following section.

It is useful to have an idea of where true coincidences are expected to occur in the excitation spectrum of ^{16}O. At the proton energy of 902 keV, we expect to be resonant on the 12.97 MeV state in ^{16}O. Hence, we expect this to be the excitation energy in ^{16}O for α_0-coincidences if the α decay of the 12.97 MeV state to the ground state were not forbidden. Additionally, α_1-coincidences are expected to be located 4.44MeV lower than α_0-coincidences, at 8.53 MeV. The excitation spectrum of ^{16}O is plotted in Figure 3.11 for the 902 keV experiment. Two distinct peaks are clearly visible a few hundred keV lower than the expected values. Hence, we can conclude that the presence of an α_0 peak indicates that we are also populating the two nearby natural states, mentioned in Section 3.2.

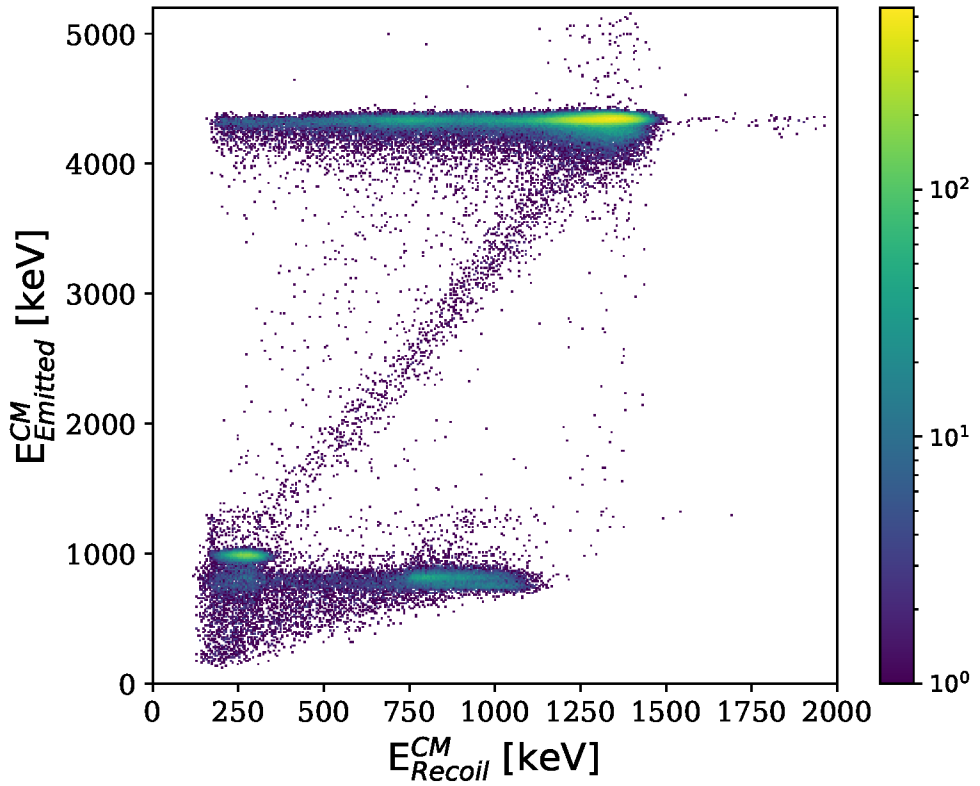

FIGURE 3.10: The center of mass energy of the emitted particle plotted against the energy of the recoil particle for the 902 keV experiment.

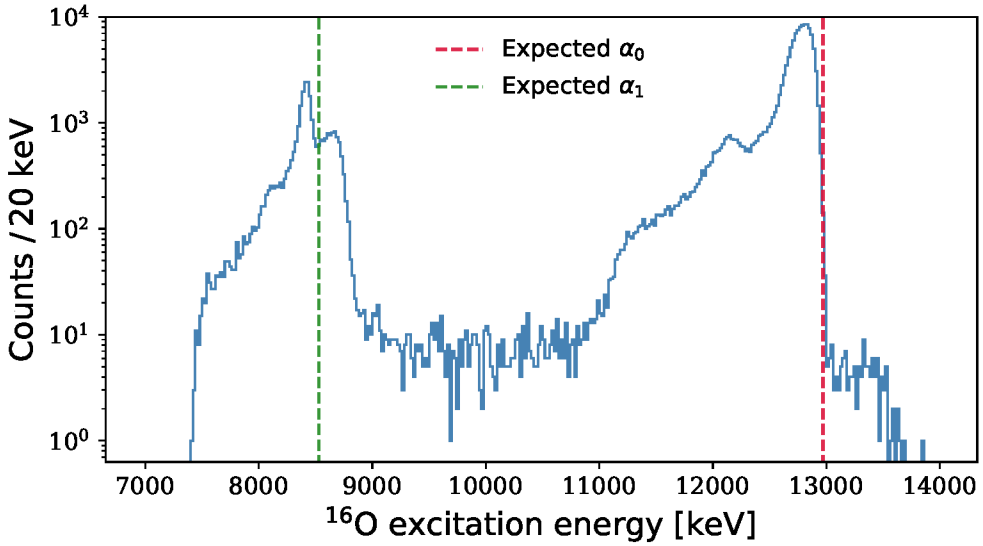

FIGURE 3.11: The excitation spectrum of the 902 keV experiment. The expected positions of the α_0 and α_1 peaks are shown.

Cuts

The first cut applied is on the net momentum, which should add up to zero in the center of mass. Figure 3.12A shows the total momentum in the center of mass plotted against the excitation energy for the 902 keV experiment. Fortunately, the peaks located at the expected α-coincidence values are centered at lower values of the total momentum. The α_0 peak has a tail extending up to 130 MeV/c. This tail is believed to consist of true coincidences with incorrect energy measurement of ^{12}C, as evident from the large spread on the recoil energy of the top peak in Figure 3.10. A cut at 50 MeV/c is made to remove as much of the elastic scattering of protons around the α_1 peak as possible while preserving the main α_0 peak. If this discrepancy was purely due to an incorrectly measured energy of the α, the momentum cut corresponds to the energy being wrong by $\approx$335keV.

The second cut is on the total angle in the center of mass, which must be 180 degrees for the α and ^{12}C to be emitted back-to-back as expected. As shown in Figure 3.12B, a cut at 163 degrees is placed to preserve most of both peaks.

The third and final cut is a time cut. ^{12}C is expected to be detected a few nanoseconds after the α due to its larger mass. In Figure 3.12C the time difference between the two detections is plotted. A cut is placed to accept ^{12}C to be detected 35 ns after and 20 ns before the α.

A suspicious amount of data with $T_C - T_\alpha = 0$ is seen in Table 3.4.C, making up 6.6% of the total data before the cuts and 4.0% after the cuts. A quick check showed that this is not because of the two particles being detected at the exact same time, but rather because the TDC, for yet unknown reasons, has time-stamped both particles with $T = 0$ within their event. The same anomaly was seen in the 1028 keV experiment.

In Section 3.5.3, I will elaborate on the characteristics of this suspicious subset of the data. Until then, this anomaly will be dealt with by separating the search for potential γ-delayed α_0-coincidences into two cases:

1. Using all data with the cuts applied, referred to as *'All'*.
2. Similar to 1. but excluding the data that got time-stamped to zero, referred to as *'$T \neq 0$'*.

The cuts that have been presented here are listed in Table 3.4 along with the cuts used for the 1028 keV experiment.

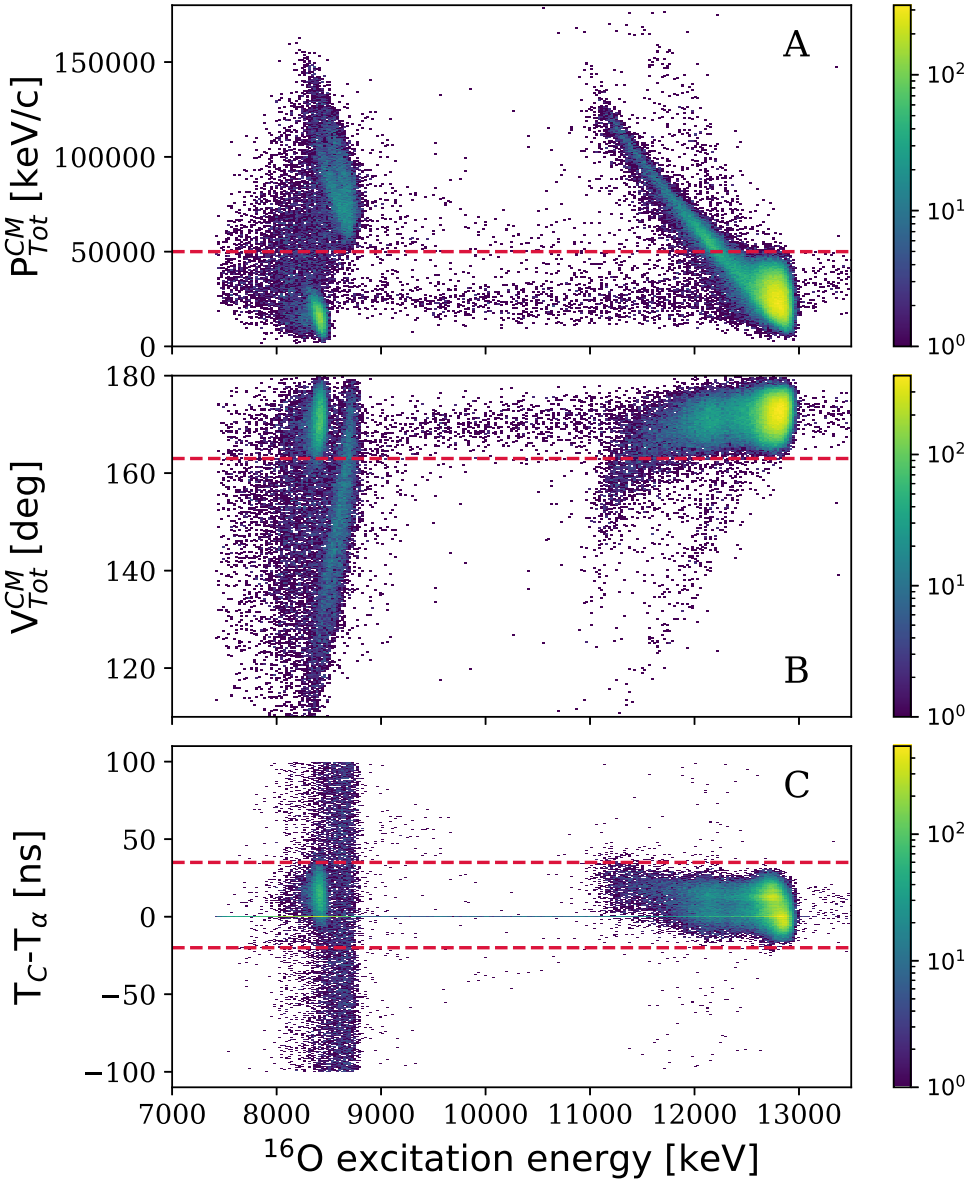

FIGURE 3.12: (A) The total center of mass momentum, (B) total angle in the center of mass, and (C) the detection time difference plotted against the excitation energy in ^{16}O for the 902 keV experiment. The dotted red lines represent the imposed cut. Similar plots for the 1028 experiment is shown in Appendix A.

TABLE 3.4: Kinematic constraints imposed on the 902 and 1028 keV experiment.

	P^{CM}_{Tot} [MeV/c]	V^{CM}_{Tot} [deg]	T_C−T_α [ns]
902 keV	<50	>163	>-20 , <35
1028 keV			>-18 , <30

3.5 Results

In this section, I will present the process and results of identifying the potential γ-delayed α_0 coincidences using the 902 keV experiment throughout. Similar plots for the 1028 keV experiment can be found in Appendix A.

3.5.1 Identifying γ-delayed α decays

By using Equation (2.5) and $Q = T_\alpha + T_C$, it is fairly straightforward to demonstrate that the kinetic energy of the α and ^{12}C nucleus scale linearly according to

$$T_\alpha = \frac{m_C}{m_\alpha} T_C = 3T_C. \tag{3.4}$$

Therefore, as there is less energy available for the two particles, γ-delayed α_0-coincidences are expected to appear as a band following Equation (3.4) below the α_0 peak in a plot of the energy of the α versus the energy of the ^{12}C nucleus. This plot is shown in Figure 3.13 for the two cases. The expected energies of α-coincidences are included which were calculated using Equation (2.5).

First, the All case shows a band of coincidences between the α_0 and α_1 peaks. The parameterization that is used to confine these candidates is

$$\begin{aligned} -100\text{keV} < E_\alpha - 3E_C < 600\text{keV}, \\ 1200\text{keV} < E_\alpha < 4100\text{keV}. \end{aligned} \tag{3.5}$$

A total of 1941 candidates are confined in this area. However, notice that the upper limit on E_α has been chosen quite generously, where some of the α_0-shoulder is almost certainly included. This is due to the expectation of γ-delayed α_0-coincidences, particularly through the 12.44 and 12.05 MeV states, to be in this area.

Looking at the $T \neq 0$ case in Figure 3.13, a major part of the candidates disappear. With the same parameterization, a total of 599 candidates are still present. Of these, 98% are above $E_\alpha^{CM} = 3700$ keV and are arguably part of the α_0-shoulder. Unfortunately, this trend is also observed in the 1028 keV experiment.

The excitation spectrum of the γ-delayed α_0 candidates is shown in Figure 3.14. The energy of the states we wish to populate through γ decay in ^{16}O are indicated with arrows. Recalling that we included some of the α_0-shoulder

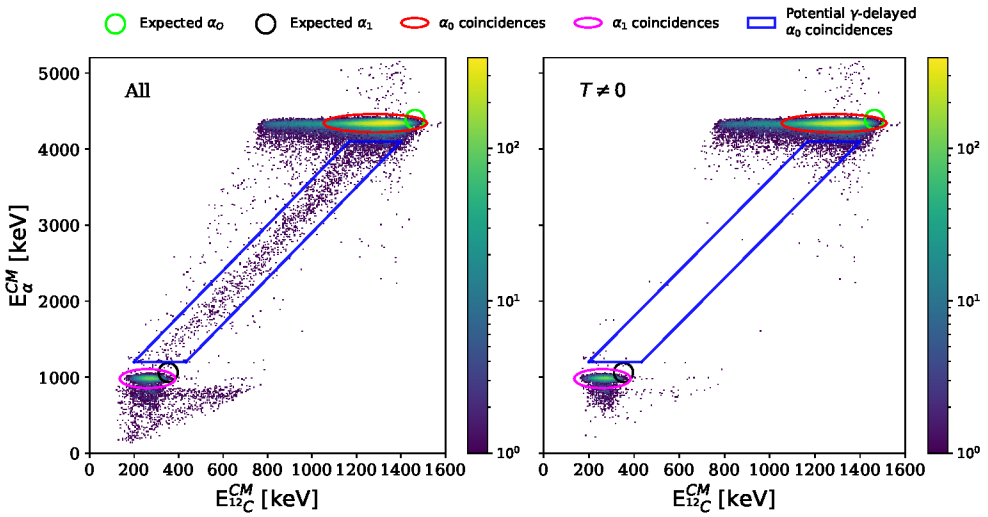

FIGURE 3.13: The center of mass energy of the α plotted against the energy of the ^{12}C nucleus for All (left) and T $\neq$ 0 (right) in the 902 keV experiment. Expected values of α_0 and α_1 decays are indicated with circles, while the actual peaks are indicated with ellipses. The data within the blue box are potential candidates of γ-delayed α_0-coincidences.

in the confined area, no significant peaks are observed in the vicinity of the states in either of the two cases.

3.5.2 Radiative decay widths

As a consequence of the above, it is not feasible to determine exact information about the γ-decays from the 12.97 or 13.09 MeV states to the natural parity state above the α separation energy in ^{16}O. Instead, I will use the lack of candidates to set upper limits on the radiative decay widths.

The radiative decay widths from the parent state to the i-th excited state can be calculated using the corresponding branching ratio and the known total decay width of the parent state. The branching ratio from the parent state to the i-th excited state is

$$B_i = \frac{N_i}{\epsilon_i N_P}, \tag{3.6}$$

where N_i is the number of γ decays to the i-th state and ϵ_i is the efficiency coefficient describing the efficiency of the detection setup to detect the following α_0-coincidence. N_P is the total number of populations of the parent state. This

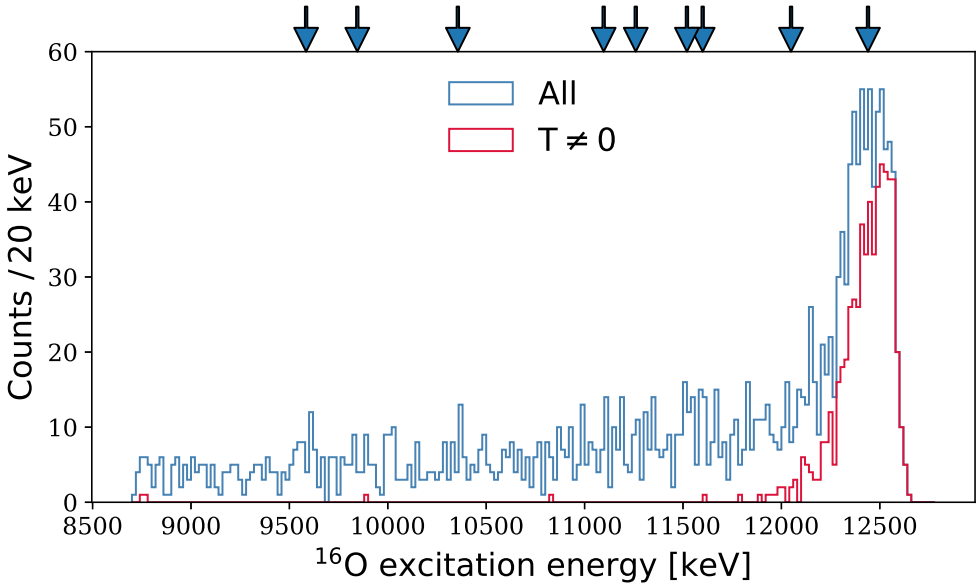

FIGURE 3.14: The excitation spectrum of the γ-delayed α_0 candidates for the two cases in the 902 keV experiment. The arrows indicates the states in Table 3.1.

can be determined using one of the α peaks through

$$N_{\mathrm{P}} = \frac{N_\alpha}{\epsilon_\alpha \left(\Gamma_\alpha / \Gamma_{\mathrm{tot}}\right)}. \tag{3.7}$$

Here, N_α/ϵ_α is the number of α decays, and $\Gamma_\alpha/\Gamma_{\mathrm{tot}}$ is the branching ratio of the specific α decay of the parent state. Combining Equation (3.6) and Equation (3.7), the radiative decay width from the parent state to the i-th excited state is:

$$\Gamma_{\gamma,i} = \Gamma_{\mathrm{Tot}} B_i = \frac{N_i \epsilon_\alpha}{N_\alpha \epsilon_i} \Gamma_\alpha. \tag{3.8}$$

In principle, it is irrelevant which of the two α peaks is used to determine the radiative decay widths in Equation (3.8). However, as previously noted, the 12.97 MeV state is non-resonant to the ground state of ^{12}C, making the α_1 peak our only option. Selection rules do not forbid α_0 or α_1 decay from the 13.09 MeV state. Despite this, Γ_{α_1} has yet to be determined, so the α_0 peak will be used. The relevant decay widths are listed in Table 3.5.

The efficiency coefficients were obtained by simulating 10^6 reactions for each decay channel using simX. The fraction of detected coincidences using the same setup as in the experiments then gave the efficiency coefficients. The cuts were also imposed to take into account any biases. An example of a reaction file is shown in Appendix A. The line shape of ^{16}O after the γ decay

TABLE 3.5: α decay widths and total decay width of the parent states populated in the 902 keV (12.97 MeV) and 1028 keV (13.09 MeV) experiments. Values from [20]. (nr = non-resonant, r=resonant).

E_x [MeV]	Γ_{α_0}[keV]	Γ_{α_1}[keV]	Γ_{Tot}[keV]
12.97	nr	0.30 ± 0.06	1.47 ± 0.04
13.09	40	r	140 ± 10

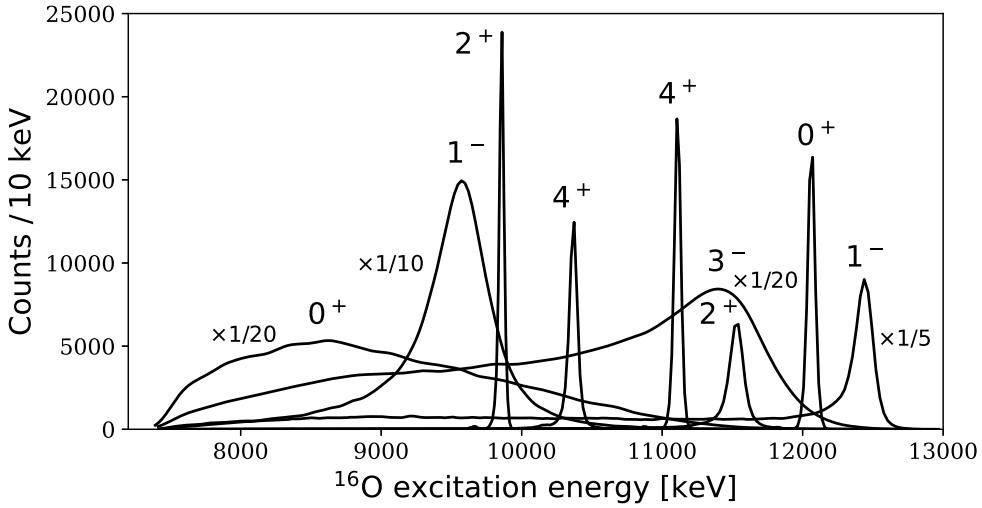

FIGURE 3.15: Simulations of γ-delayed α decay of the 12.97 MeV state through all nine states listed in Table 3.1. Notice the different scalings.

was given a Breit-Wigner shape multiplied with the gamma phase space factor, proportional to E_γ^{2L+1} (see Equation (2.10)). The subsequent α and ^{12}C were given a Breit-Wigner shape taking into account the Coulomb penetrability factor. The final line shape of the γ-delayed α decay of the 12.97 MeV state through all nine excited states is shown in Figure 3.15.

Determining N_i was more challenging than anticipated due to two reasons: (1) Correctly estimating the number of candidates that went through a particular excited state was difficult due to the wide decay widths of some excited states; this resulted in difficulty in confidently assigning a candidate to a single excited state. (2) Finding correct methods that also gave useful (i.e low) upper limits was also a challenge.

In the end, the method used for the estimation utilized the excitation spectrum of the excited states obtained from simulations (those shown in Figure 3.15). The method can be described in two steps:

1. The simulated excitation spectrum of the i-th excited state was normalized with its peak value, resulting in a spectrum that served as weights; for every bin in the spectrum, it states the likelihood of detecting a candidate through the i-th excited state in that bin.

2. The excitation spectrum of the candidates in the experiment was multiplied bin-wise by the corresponding weight and the resulting spectrum was then summed to give the estimate of the number of candidates going through the i-th excited state.

These two steps were repeated for all nine excited states. It is worth noting that this method resulted in non-integer values for the number of candidates going through a certain excited state.

Due to the high N_i values obtained for γ-delayed α decays through the 12.44 MeV state, caused by the inclusion of the α_0-shoulder, an exponential curve was fitted and subtracted from all the candidates above $E_x(^{16}O) = 12$ MeV before the estimation method was applied, for both the All and $T \neq 0$ cases.

Finally, the observed number of γ-delayed α decays was converted to upper limits on the mean value. Assuming the number of decays to be Poisson distributed, the $(1 - a)$ confidence level (CL) upper limit is

$$N_i^{\text{mean}} \leq \frac{1}{2}\chi^2_{2(N_i^{\text{observed}}+1),1-\frac{a}{2}}\,, \tag{3.9}$$

where $\chi^2_{\text{df},x}$ is the cumulative distribution function of the χ^2 distribution with df degrees of freedom, evaluated at x [29]. This expression is not simply linear with respect to df and hence not to N_i^{observed}. Therefore, it matters whether we define the number of observed candidates, N_i^{observed}, as the number of detections, N_i, or the number of events that are expected to have happened, N_i/ϵ_i. After much consideration, the latter was used as that gives a larger number of candidates to use in the statistical calculation, thus resulting in lower upper limits in the end.

Using the formula in Equation (3.8) to compute the radiative decay widths, we can safely propagate the CL on N_i/ϵ_i to the Γ_γ values, as the statistics that went into calculating the $N_{\alpha_1}/\epsilon_{\alpha_1}$ is so high that determining lower limits on this value would not significantly alter the final result.

The 90% CL upper limit on the radiative decay widths computed with Equation (3.8) are tabulated in Table 3.6 for the two cases.

TABLE 3.6: 90% CL upper limits on radiative decay widths and branching ratio for the transitions from the 12.97 and 13.09 MeV states to natural parity states in ^{16}O above the α separation energy. These upper bounds have been calculated for both the All and T $\neq$ 0 cases.

Initial state (MeV, J^π)	Final state (MeV, J^π)	Γ_γ (eV)		$\Gamma_\gamma/\Gamma_{\text{Tot}}$ ($\times 10^{-4}$)	
		All	T $\neq$ 0	All	T $\neq$ 0
12.97, 2^-	12.44, 1^-	0.95	0.041	6.5	0.28
	12.05, 0^+	0.85	0.043	5.8	0.29
	11.60, 3^-	14	0.20	92	1.4
	11.52, 2^+	1.4	0.010	9.2	0.071
	11.26, 0^+	9.7	0.099	66	0.67
	11.10, 4^+	0.53	0.0083	3.6	0.056
	10.36, 4^+	0.47	0.0079	3.2	0.054
	9.84, 2^+	0.24	0.0075	1.6	0.051
	9.59, 1^-	2.8	0.021	19	0.14
13.09, 1^-	12.44, 1^-	32	3.1	2.3	0.22
	12.05, 0^+	7.7	0.77	0.55	0.055
	11.60, 3^-	86	1.9	6.1	0.13
	11.52, 2^+	7.5	0.61	0.54	0.043
	11.26, 0^+	85	2.2	6.1	0.16
	11.10, 4^+	3.2	0.12	0.23	0.0089
	10.36, 4^+	5.2	0.12	0.37	0.0089
	9.84, 2^+	1.9	0.12	0.14	0.0088
	9.59, 1^-	17	0.25	1.2	0.018

3.5.3 Characteristics of incorrect time-stamped data

A significant portion of the α particles and ^{12}C nuclei that might have resulted from γ-delayed α decay were recorded by the TDC as occurring simultaneously at $T = 0$ within their event. This incorrect time-stamping could be attributed to various signal processing issues such as pile-up, saturation, etc. In this section, I will present three observed features of this subset of the data, which will ultimately lead to a hypothesis of why the TDC mistakenly recorded some of the data.

First, the data with $T = 0$ is not only found in the γ-delayed α decay region but rather it is distributed throughout the entire excitation spectrum as illustrated in Figure 3.16. At the α peaks, it constitutes $2 - 5\%$ of the total data, whereas makes up almost all of the data in the inter-peak regions.

The second characteristic is that $T = 0$ data were significantly more likely to come from events with multiplicities above two than the rest of the data, as

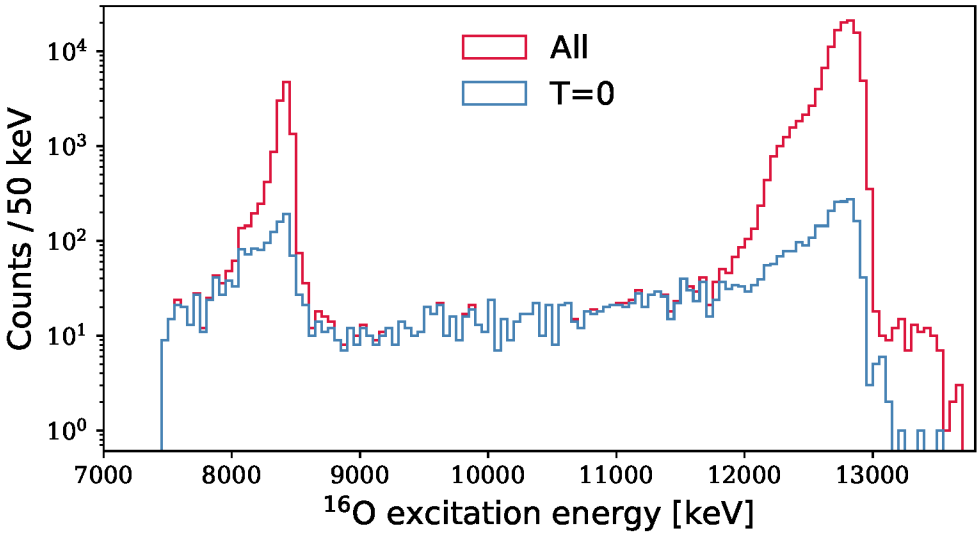

FIGURE 3.16: Excitation spectrum of $T = 0$ data for the 902 keV experiment. For comparison, the excitation spectrum for all data is also shown.

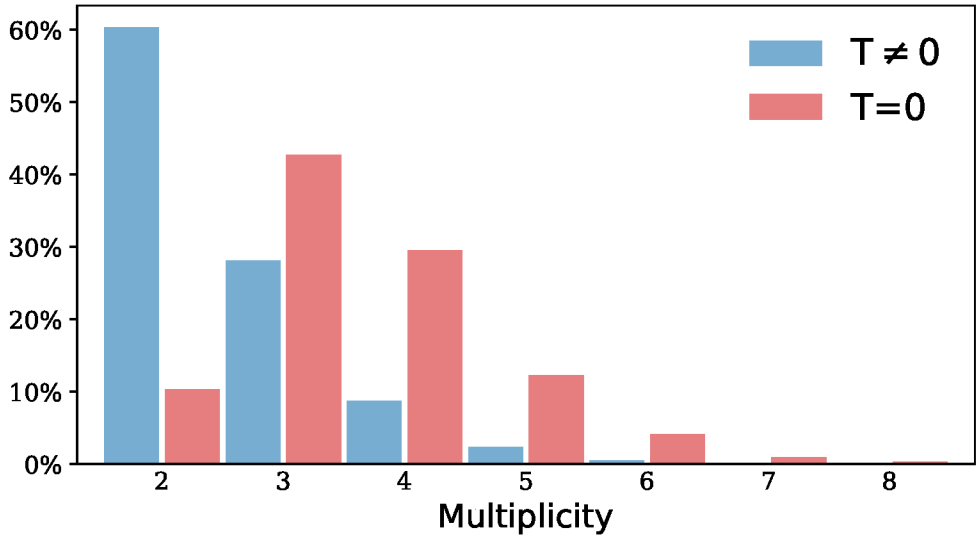

FIGURE 3.17: Multiplicity distribution of the 902 keV experiment without the cuts imposed. The data is divided into two subsets, with and without $T = 0$ data, and the amount of counts for a given multiplicity is divided by the total amount of counts within that subset to give the normalized number of counts.

shown in Figure 3.17. Only 10% of the $T = 0$ data originated from events with two particles detected within the event, compared to 60% for the rest of the data.

Third, due to fluctuations in the beam current throughout the experiments, the trigger rate also varied and there is approximately a linear correlation

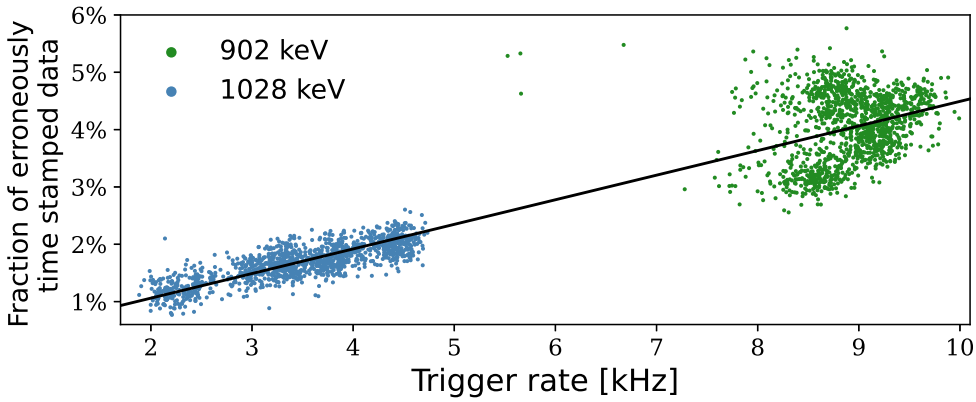

FIGURE 3.18: The fraction of the total data that got incorrectly time-stamped as a function of the trigger rate. Each data point represents a 5 seconds interval of the given experiment. A least square linear regression gave $y = 4.3 \times 10^{-3}x + 2.02 \times 10^{-3}$ with $R^2 = 0.88$.

between the trigger rate and the ratio of observed $T = 0$ data. This was realized by dividing the experiments into 5 second intervals, calculating an average trigger rate and the fraction of $T = 0$ data (as observed in the sorted file) in each interval, and plotting the result in Figure 3.18. The correlation is evident in the 1028 keV experiment and can be seen, albeit with some fluctuations, in the 902 keV experiment too. There seemed to be a couple of sudden shifts in the fraction of $T = 0$ throughout the 902 keV experiment, such that 97% of the data from the first quarter of the experiment ended up beneath the linear regression line, while 98% of the data from the last quarter is above it. What caused these shifts is still not understood fully. Nevertheless, a linear correlation is still fairly obvious with a reasonable R^2 value of 0.88.

With the question of the anomaly's origin remaining, I propose that these are actually pure α-coincidences based on the three key observations. However, these were detected in events that were triggered by the tremendous amount of scattered protons in the SD. If the data collection gate closed just as the signals from the α and ^{12}C were being integrated by the ADC, the measured energy would decrease by roughly the same factor as their signals were almost simultaneous. This is exactly what is observed with a large part of the $T = 0$ data. What specifically caused the TDC to time-stamp these hits with zero is unclear, but somehow it must have been confused and given a dummy value.

This hypothesis also explains the high occurrence of $T = 0$ in events with a multiplicity of more than 2 and the results seen in Figure 3.18 as the amount

of $T = 0$ data would increase with the increase of beam current, leading to more scattered protons in the SD.

3.6 Discussion

The above analysis suggests that the $T = 0$ data can safely be discarded and hence we interpret the results from the $T \neq 0$ case as the true results. Thus the presented experiments have been sensitive to radiative decay widths down to 7.5 and 120 meV for the 902 and 1028 keV experiment, respectively.

As expected, the sensitivity of the presented experiments is not adequate to set sensible upper limits on transitions with multipolarity $L > 1$, as it is not enough to detect the small γ branches expected by the Weisskopf estimates to be in the range of 10^{-2}-10^{-7} meV. A significant improvement in sensitivity, by several orders of magnitude, would be required to detect these branches.

We were able to set sensible upper limits on the dipole transitions, for which there exist no literature values so far. Of special interest is the dipole transitions to the 9.84 and 9.59 MeV states, and thus the upper limits on their radiative decay widths are shown in units of the Weisskopf estimates in Table 3.7. Unfortunately, the upper limits are up to four orders of magnitude smaller than expected by the Weisskopf estimates, indicating that the transition is slowed down by a poorer match-up of the initial and final wave functions than expected by the Weisskopf approximation. Hence, it seems like to detect the population of these two states from the 12.97 and 13.09 MeV states, an improvement in sensitivity is necessary.

The IDOG method has been used in previous studies by Munch et al. [13] and Kirsebom et al. [11] to measure radiative decay widths of a few meV. Despite studying four-particle coincidences with a 38% detector coverage, Kirsebom et al. achieved a great sensitivity by increasing the measurement time to 18 hours. Similarly, Munch et al.'s results were based on almost a week's worth of measurements.

One positive aspect of the present study is that, although no significant population of the desired final state was detected, the area where we would expect them to appear if the sensitivity was increased is basically background-free, as shown in Figure 3.14 for the $T \neq 0$ case. This nicely demonstrates one of the main benefits of the IDOG method, as increasing sensitivity does not result

TABLE 3.7: Upper limits on the radiative decay widths in Weisskopf units for the dipole transitions to the 9.59 and 9.84 MeV states.

Initial state (MeV, J^π)	Final state (MeV, J^π)	Γ_γ (W.u.)
12.97, 2^-	9.84, 2^+	5.7×10^{-4}
	9.59, 1^-	2.6×10^{-2}
13.09, 1^-	9.84, 2^+	8.0×10^{-3}
	9.59, 1^-	0.28

in an increase of an inherent background, as is the case with conventional γ spectroscopy, setting a lower threshold on γ branches that can be measured.

In the future, two approaches can be taken to improve the results of this study. The first is to calculate precise theoretical radiative decay widths using an ab initio or shell model to determine the reduced transition probabilities. The second approach is to improve the experimental sensitivity. This can be done by increasing the measurement time, increasing the detector solid angle coverage by including the SU and SD, or fixing the issue with the TDC to increase the sensitivity on the radiative decay width. If a longer measurement time of a week was possible, the sensitivity would be improved by roughly two orders of magnitude, allowing the detection of $10^{-1} - 10^{-2}$ meV widths. Increasing the detector solid angle coverage by including the SU and SD could increase the sensitivity by a factor of 1.4, although stricter cuts would need to be applied to account for increased Rutherford scattering, effectively reducing this improvement slightly. Fixing the issue with the TDC could also improve sensitivity by roughly 4%, as the incorrect time-stamped data is expected to be true α_0 coincidences, which could have contributed to the α_0 peak, which was used to compute the radiative decay width.

Finally, it is worth mentioning that it was intended to repeat the presented experiments with longer measurement times. Unfortunately, due to issues with the DAQ at the accelerator facility starting in the summer of 2022, it was not possible to do so.

Chapter 4

γ decay in ^{8}Be

4.1 Motivation

The solar neutrinos produced from the β^+ decay of ^{8}B to ^{8}Be played a crucial role in resolving the solar neutrino problem, revealing that neutrinos oscillate between different flavor states as they travel from the Sun to Earth. This decay happens as part of one of the branches of the proton-proton chain in low-mass main sequence stars and is the major source of solar neutrinos with energies higher than modern neutrino detector threshold of a few MeV. To better understand this quantum phenomenon, extensive efforts have been made to measure the ^{8}B neutrino spectrum [30, 31].

In Figure 4.1, the decay of ^{8}B is illustrated. ^{8}Be has five states within the relevant energy range [32]. The decay to the ground state 0^+ and the broad state at 11.4 MeV (4^+) are both second forbidden and hence highly suppressed. The decay will mainly populate three 2^+ resonances in ^{8}Be. These are the 1.5 MeV broad state at 3.0 MeV (2^+_1) and two narrow states at 16.6 and 16.9 MeV (2^+_2 and 2^+_3) with decay widths of 108 and 74 keV, respectively. Thus, ^{8}B decays to a continuum of states primarily centered around the broad 3.0 MeV state, which ultimately is responsible for the shape of the neutrino spectrum. Since ^{8}Be is unstable, it will subsequently break up into two α particles with a half-life of $\approx 10^{17}$s.

The two narrow states at 16.6-16.9 MeV are unique in that they are maximally mixed in isospin. The energy eigenstates $\psi_{16.6}$ and $\psi_{16.9}$ are a mixing of the isospin eigenstates $\phi_{T=0}$ and $\phi_{T=1}$, forming an isospin mixed doublet. The

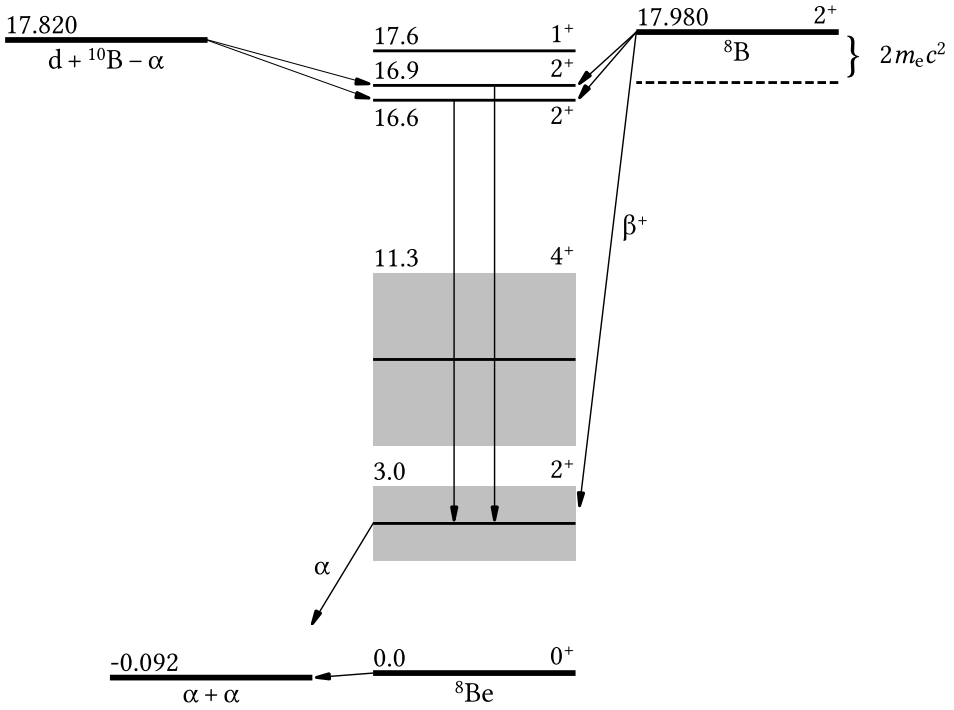

FIGURE 4.1: Level diagram of the low-energy region of ^{8}Be. Energies are in MeV and spin-parity are indicated for each level, and broad levels have their width marked with grey. The β^{+} decay of ^{8}B to the 2^{+} states in ^{8}Be is depicted. The population of the isospin doublet through the reaction $d + {}^{10}\mathrm{B} \rightarrow \alpha + {}^{8}\mathrm{Be}$ with the subsequent γ-delayed α decay through the 2^{+}_{1} state is also shown.

mixing parameters α and β are used to express this relationship as

$$\psi_{16.6} = \alpha\phi_{T=0} + \beta\phi_{T=1}, \quad \psi_{16.9} = \beta\phi_{T=0} - \alpha\phi_{T=1}, \tag{4.1}$$

with $\alpha^2 + \beta^2 = 1$. In this way, $\phi_{T=1}$ can be viewed as forming an isospin triplet along with the 2^{+} ground states of ^{8}Li and ^{8}B.

As it turns out, the most important correction term to the determination of the neutrino spectrum from experimental data is called the weak magnetism term. To first order, this term arises from an interference between the Gamow-Teller contribution of the β decay to the 2^{+}_{1} state and the magnetic dipole contribution from the ^{8}Be analog state of the ^{8}B ground state ($\phi_{T=1}$) to the 2^{+}_{1} state. The current best description of the neutrino spectrum assumes an energy dependence of the weak magnetism which is related to the isovector (ΔT= 1) radiative M1 decay width of the isospin doublet [33]. For more information on weak magnetism, I refer to the work of Wang et al.[34]

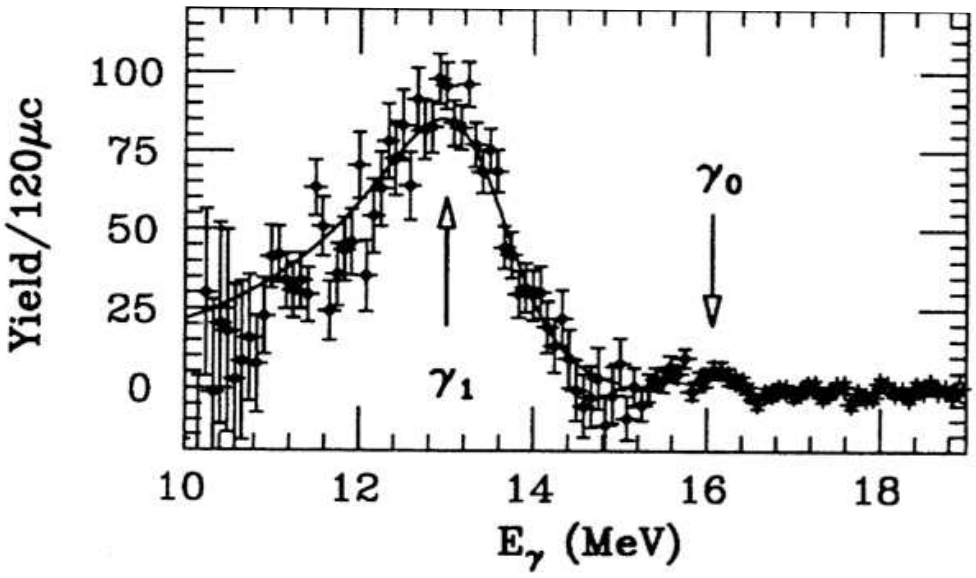

FIGURE 4.2: Gamma spectrum from the decay of the 2^+_3 state measured with a conventional NaI detector. The γ_1 and γ_0 peaks correspond to the decay to the first excited state, 2^+_1, and the ground state, respectively. The smooth curve is an R-Matrix fit to the $2^+_3 \rightarrow 2^+_1$ transition. Figure from [33].

To improve the accuracy of the neutrino spectrum, De Braeckeleer et al. used the ^{4}He(α,γ)^{8}Be reaction and a NaI detector to measure the $2^+_{3,2} \rightarrow 2^+_1$ γ decay. The results from the decay of the 2^+_3 state are shown in Figure 4.2. The main peak (γ_1) is the M1 transition to 2^+_1 and the smaller peak (γ_0) is the E2 transition to the ground state. The bad energy resolution of NaI detectors gives the data a large uncertainty in energy. Furthermore, the uncertainty in the yield increases quite drastically when approaching γ energies of 10 MeV.

In order to resolve these issues, an experiment has been proposed at the Centre for Micro Analysis of Materials (CMAM) in Madrid. The experiment will explore the ^{10}B(d,α)^{8}Be transfer reaction which has previously been observed to populate the isospin doublet with a good cross section ($\approx$ 10 mb at 7.5 MeV beam energy) [35]. Using the IDOG method, the γ spectrum from the doublet can be determined by measuring the subsequent 2α breakup in complete kinematics. This will allow for a more precise measurement of the γ_1 peak and extend the energy range down to at least 1 MeV.

Initially, the goal of this chapter was to analyze the data from the experiment to deduce the γ spectrum. At present, however, the experiment has not been conducted yet. Unfortunately, the experiment cannot be carried out at the Van der Graaf facility at Aarhus University as the collision of deuterium with

the various setup apparatuses produces neutrons if the beam energy is more than the separation energy of 2.2 MeV. These neutrons can cause biological damage and would interfere with other neighboring experiments.

Instead, the objective of this chapter has transformed into using Monte Carlo simulations to assess the feasibility of using the IDOG method for deducing the γ spectrum from the isospin doublet. The simulations will identify factors to consider when using the IDOG method and evaluate the reliability of the results. Additionally, simulations will be used to determine the detection efficiency for different deuterium beam energies.

4.2 The simulation of the reaction

In the following, the decay channel we want to simulate will be referred to as the γ-delayed 2α breakup. It is

$$d + {}^{10}\mathrm{B} \rightarrow \alpha + {}^{8}\mathrm{Be}^{*}(2_3^+/2_2^+) \rightarrow \alpha + \gamma + {}^{8}\mathrm{Be}^{*}(2_1^+) \rightarrow \alpha + \gamma + \alpha + \alpha, \qquad (4.2)$$

and is shown in Figure 4.3 in both the lab and center of mass frame of the beam-target system, i.e. the $d + {}^{10}$B system. In the following, unless stated otherwise, we will define the center of mass as the center of mass of the beam-target system. Furthermore, we will denote the emitted α in the first decay step as the primary particle, and the two from the second decay step as the secondary particles.

To achieve a significant number of the desired transfer reactions in an experiment, the beam energy must be greater than the Coulomb barrier between deuterium and ^{10}B. According to Equation (2.6), the Coulomb barrier is 1.47 MeV.

The Monte Carlo simulation of the γ-delayed 2α breakup was carried out using the AUSAlib simulation tool, simX, which is described in Section 3.3.4. To account for the two states in the isospin doublet, separate simulations were performed. An example of the reaction file used is shown in Appendix B. 10^7 events were simulated for each case using a 2 and 7.5 MeV deuterium beam. The target was modeled as a 20 μg/cm^2 ^{10}B foil on a 4 μg/cm^2 carbon backing. The CMAM experiment will use two $\Delta E - E$ telescopes at backward angles and a Si-Ball at forward angles, which allows for good angular coverage but avoids the angles at $0 - 30$ degrees which will be dominated by Rutherford scattering.

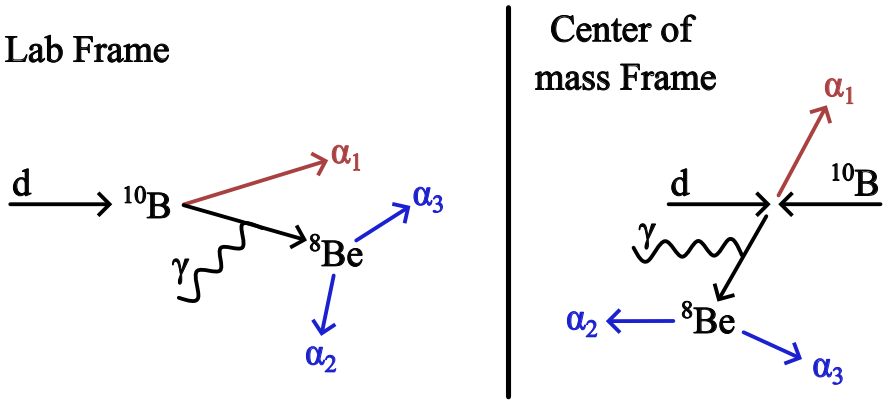

FIGURE 4.3: The transfer reaction and subsequent decay in two different frames of reference. On the left, the reaction steps are shown in the laboratory frame. To the right, the reaction steps are portrayed in the beam-target center of mass frame. It is worth noting that the two secondary particles are not emitted in a back-to-back manner in this frame, as this is only the case in the center of mass of ^{8}Be. For visual clarity, the primary α particle is depicted in red, while the secondary particles are shown in blue. For simplicity's sake, the negligible γ recoil on ^{8}Be has not been included in the figure.

However, for simplicity reasons, the simulation presented here uses the same detector setup as in Chapter 3.

The simulation can provide the actual γ energies for the γ-delayed 2α breakup, which will serve as our theoretical values when evaluating the effectiveness of the IDOG method. Initially, it was thought that only the γ energies from all 10^7 events could be extracted, meaning a scaling difference would occur with our deduced γ spectrum due to detection efficiency. To eliminate the effect of detector efficiency, we need to only compare with the theoretical γ energies of events that were actually detected in complete kinematics. Due to the way data is stored in simX, this was initially not possible, but I eventually found a solution, so it is now possible to directly assess the efficiency of the IDOG method.

The γ spectrum for two cases will be calculated for each of the two beam energies:

1. Only decay through 2^+_3 is considered.

2. Both decay through 2^+_3 and 2^+_2 are considered. This is achieved by combining the two simulation files into one file before processing through the AUSAlib pipeline.

In the former, a single spectrum will be obtained. In the latter, a separate γ spectrum for each of the two states will be calculated.

4.3 Energy consideration

If we define the energies with respect to the ground state of ^{8}Be, the energy released in the first and second decay steps are $Q_1 = E_{d+^{10}B-\alpha} - E_{^{8}Be(2_3^+/2_2^+)}$ and $Q_2 = E_{^{8}Be(2_1^+)} - E_{2\alpha}$, respectively. Then, using conservation laws (see Appendix B for derivation), the center of mass energies of the primary and two secondary particles can be expressed as

$$\begin{aligned} E_1 &= \frac{2}{3}Q_1 + \frac{5}{9}E_d, \\ E_2 &= \frac{1}{4}E_1 + \frac{1}{2}Q_2 + \cos\theta\sqrt{\frac{E_1 Q_2}{2}}, \\ E_3 &= \frac{1}{4}E_1 + \frac{1}{2}Q_2 - \cos\theta\sqrt{\frac{E_1 Q_2}{2}}, \end{aligned} \tag{4.3}$$

where E_d is the deuterium beam energy in the laboratory frame, θ is the angle between the ^{8}Be in the center of mass and one of the secondary particles in the center of mass of ^{8}Be. Taking the decay through 2_3^+ as an example, the γ-delayed 2α breakup have $Q_1 = 0.9$ MeV and $Q_2 = 3.1$ MeV and so $E_1 = 1.7$ MeV and $0.6 < E_{2,3} < 3.3$ MeV. However, the non-zero decay width of 2_3^+ results in a broadening of the primary particle energy around 1.7 MeV. Similarly, the large decay width of 2_1^+ allows the secondary particle energy to exceed the stated range. It's also worth noting that the primary and secondary particle energies overlap.

The IDOG method can determine the energy of the γ from the energy of the primary and secondary particles. As an example, consider the decay through the 2_3^+ state. We have

$$E_\gamma = E_{2_3^+} - E_{2_1^+}. \tag{4.4}$$

$E_{2_3^+}$ can be expressed as a function of known variables using the formula for E_1 in Equation (4.3) as

$$E_{2_3^+} = E_{d+^{10}B-\alpha} + \frac{5}{6}E_d - \frac{3}{2}E_1. \tag{4.5}$$

Moreover, the excitation energy in ^{8}Be before the 2α breakup, $E_{2_1^+}$, can be determined through the invariant mass method (Equation (3.3)) using the four-momentum of the two secondary particles in the center of mass of ^{8}Be. Thus,

$$E_\gamma = E_{d+^{10}B-\alpha} + \frac{5}{6}E_d - \frac{3}{2}E_1 - \left[(p_2 + p_3)^2 - m_{^8\mathrm{Be}} - 92\mathrm{keV}\right], \tag{4.6}$$

where the 92 keV is subtracted from the excitation energy since that is the difference between the 2α threshold and the ground state of ^{8}Be.

As a consequence of the above, I see two aspects that need to be considered in order to successfully detect the desired γ decays in a ^{10}B(d,α)^{8}Be experiment using the IDOG method:

1. *Gating*: Since the transfer reaction may result in ^{8}Be in any of the excited states in the low-energy region, we need to be able to gate on the events going through the 2_3^+ state and those going through 2_2^+ state.

2. *Particle identification*: In order to successfully extract a γ spectrum, we need to know which of the three α particles is the primary particle.

These two challenges will be addressed in the next two sections, starting with gating.

4.3.1 Gating

The simplest way to gate on events going through one of the doublet states is to only include events with at least one particle having a center of mass energy close to the expected primary particle energy. This is nicely visualized using the kinematic curve, which is a plot of the energy of a particle against its emission angle. In the center of mass, the energy does not depend on the emission angle and so horizontal lines or bands corresponding to the energies of the primary and secondary particle will show up.

Kinematics curves of simpler reactions

To understand this gating method, and also to perform a sanity check of our expectations of the simulation output, I will show simulations of four simpler

TABLE 4.1: The Q-values of the first and second sequential steps of reaction A-D shown in Equation (4.7), including the predicted energy values of the primary particles and secondary particles. All energies are in MeV.

	Q_1	Q_2	E_1	$E_{2,3}$
A	17.8	0.092	13.0	[2.5, 4.1]
B	14.8	3.1	10.9	[0.2, 8.4]
C	[0, 17.8]	[0.092, 17.9]	-	-
D	0.9	17.1	1.7	[5.2, 12.8]

decay channels of the ^{10}B(d,α)$\alpha\alpha$ reaction, where one of the four simulations is with $\Gamma_{2_1^+} = 0$. These decay channels are

$$\begin{aligned}
\text{A}: &\quad d + {}^{10}\text{B} \rightarrow \alpha + {}^{8}\text{Be}^{*}(\text{GS}) \rightarrow \alpha + \alpha + \alpha, \\
\text{B}: &\quad d + {}^{10}\text{B} \rightarrow \alpha + {}^{8}\text{Be}^{*}(2_1^+) \rightarrow \alpha + \alpha + \alpha \quad (\Gamma_{2_1^+} = 0), \\
\text{C}: &\quad d + {}^{10}\text{B} \rightarrow \alpha + {}^{8}\text{Be}^{*}(2_1^+) \rightarrow \alpha + \alpha + \alpha, \\
\text{D}: &\quad d + {}^{10}\text{B} \rightarrow \alpha + {}^{8}\text{Be}^{*}(2_3^+) \rightarrow \alpha + \alpha + \alpha.
\end{aligned} \tag{4.7}$$

The corresponding Q values, along with the predicted primary particle energy is shown in Table 4.1 with $E_d = 2$ MeV. The range of energy values for the secondary particle is also presented, calculated for the scenario where the energy difference between the two secondary particles is at its maximum, or $\theta = 0$. The primary and secondary energies are not included for the C reactions due to the indeterminacy of the Q values. The simulations of these reactions were carried out using the same conditions as the simulations of the γ-delayed 2α breakup and with $E_d = 2$ MeV. The kinematic curves in the center of mass are displayed in Figure 4.4.

The kinematics curves of the simulations of the four reactions show great agreement with the expectations in Table 4.1. For reactions A, B, and D, the primary particle is clearly seen at the expected energy as a narrow horizontal line, which can be used for gating events going through a specific excited state. The small 74 keV decay width of the 2_3^+ is also seen in the kinematic curve of reaction D as slight smearing of the 1.7 MeV line, as compared to the lines in reaction A and B which decays to the ground state and first excited state with zero decay width.

The kinematic curve of reaction C is similar to that of reaction B, except for the introduced 1.5 MeV decay width of the 2_1^+, which broadens the primary

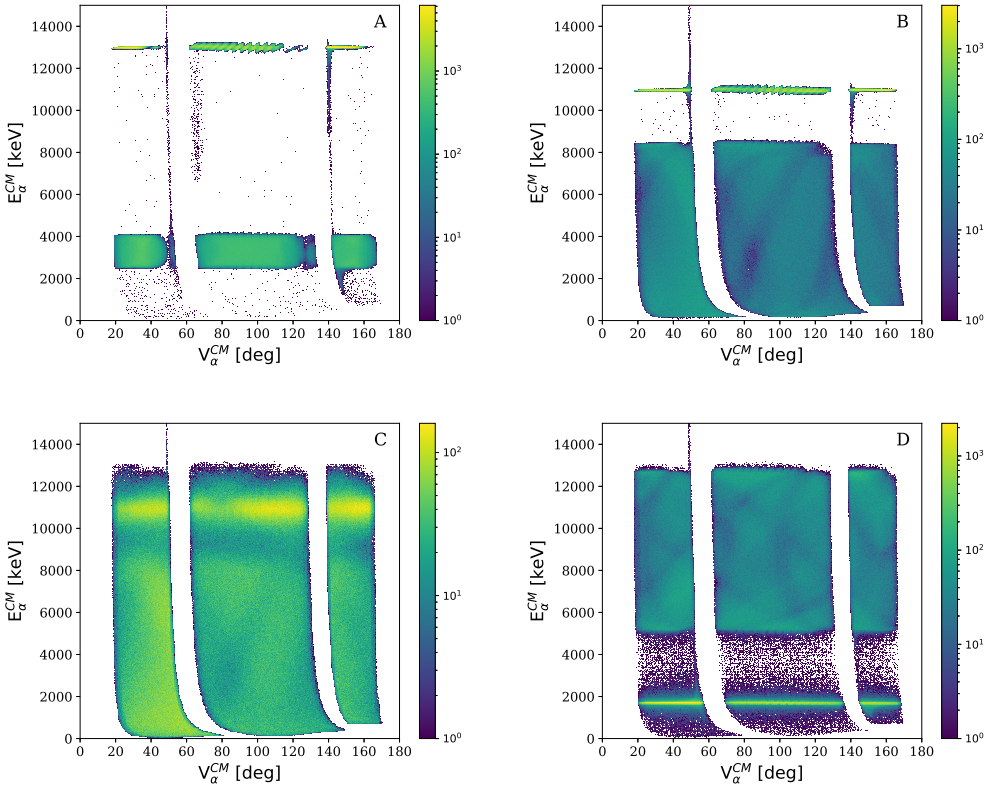

FIGURE 4.4: Center of mass kinematic curves of simulation of the four reactions, A-D, shown in Equation (4.7).

particle line and also increases the upper limit on the secondary particle energy. As a result, a clear-cut identification of what are primary particles and what are secondary particles is no longer possible. This nicely highlights the necessity for a method for particle identification which will be discussed in the next section.

Finally, two noteworthy effects are evident from the kinematic curves. Firstly, the 'jittering', particularly of the primary particle detected by Det1 and Det2 (at 65-130 degrees), is seen along the curves. This is due to the interplay between the random assignment of a hit position within a pixel when a particle hits it and the subsequent center of mass boost, as there are 16 'jitters'; exactly the number of strips on one side of Det1 and Det2. This effect is most pronounced for high-energy particles in Det1 and Det2 and least noticeable for low-energy particles in SD and SU. Secondly, a vertical spread is apparent near the outer edges of the SD and SU. The root cause of this effect is still not completely understood, but it has been narrowed down to being related to the energy correction.

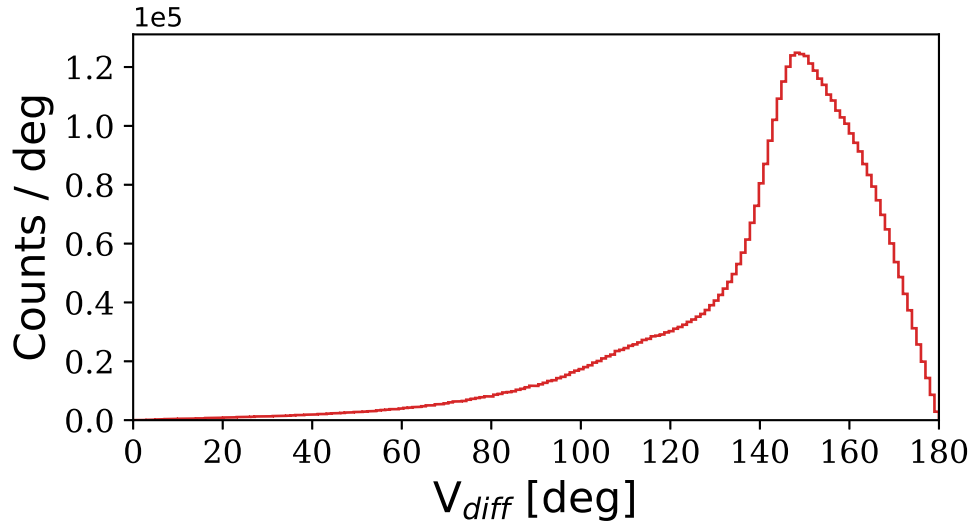

FIGURE 4.5: For the γ-delayed 2α breakup through the 2_3^+ ($E_d = 2$ MeV), the angular difference between every combinatory pair in their center of mass. The expected peak near 180 degree (secondary-secondary pairs) is not present.

4.3.2 Particle identification

To differentiate between primary and secondary particles, two approaches can be taken: either identify the primary particle or identify the secondary particles. The best method for identifying the primary particle is essentially identical to the gating method: Assign the α particle with the center of mass energy closest to the expected mean energy within an event as the primary particle. This is undeniably not a perfect method. In particular, it will be prone to make a wrong assignment if the actual primary particle ends up in the tails of the 2_2^+ or 2_3^+ states. In the following, the two methods that were considered for identifying secondary particles will be treated.

The first method was to utilize that in the center of mass of ^{8}Be, the secondary particle is emitted back-to-back. In this method, all three combinatory pairs were boosted to their center of mass and the difference in emission angle of each pair was calculated. The pair with the closest difference to the expected 180 degrees was considered the secondary particles. This method was applied to a simulation of the γ-delayed 2α breakup, and the resulting ^{8}Be excitation spectrum calculated with the two assigned secondary particles looked reasonable. However, an unexpected asymmetrical peak at 147 degrees instead of the expected peak near 180 degrees was observed in the plot of the angular difference between every combinatory pair in their center of mass

(see Figure 4.5). Despite several checks of the implemented analysis code, the origin of this discrepancy couldn't be found. From comparing the result of the method on the reactions in Equation (4.7), it seems the issue may arise when including the γ decay, although the γ recoil ($\approx$ 10 keV) is much lower than the energy resolution and should not impact the results significantly.

The second method considered was to calculate the excitation energy of ^{8}Be for every combinatory pair and then assign the pair that gives the excitation energy closest to the expected 3.1 MeV as the secondary particles. However, this method was discarded due to the large decay width of the 2_1^+ state. The effect of this large decay width is demonstrated in Figure 4.6 for the γ-delayed 2α breakup. Here, the excitation energy for two out of the three combinatory pairs is plotted against each other. This plot is also called a Dalitz plot and is shown for six different simulations with different values of $\Gamma_{2_1^+}$, starting out at 0 MeV and increasing with 0.3 MeV so that the last simulation has the actual decay width of 1.5 MeV. Looking at the simplest case, $\Gamma_{2_1^+} = 0$ MeV, then if any of the two shown excitation energies stem from a correct pairing, data will show up at the expected 3.1 MeV, which gives us the cross structure. The diagonal band corresponds to the true pairing being the one that is not presented in the plot. Since these bands are so well-defined, identifying the secondary particles based on the excitation energy should be relatively successful. However, as seen in the figure, as the decay width increases, the bands in the plot become broader, overlap more, and become less well-defined, making it difficult to identify secondary particles based on the excitation energy. The cross structure, which appeared at $\Gamma 2_1^+ = 0$ MeV, is lost at the full decay width of 1.5 MeV.

In conclusion, the method of using excitation energy to identify secondary particles was unsuccessful and using the back-to-back emission method provided suspicious results. Thus, the method of identifying primary particles through the center of mass energy was chosen for particle identification. Unfortunately, a comparison of the methods on simulated data with actual information was not possible due to limitations with simX.

4.4 Detector efficiency simulations

As an add-on to the main objective of this chapter, Monte Carlo simulation was also conducted to determine the detector efficiency at beam energies between

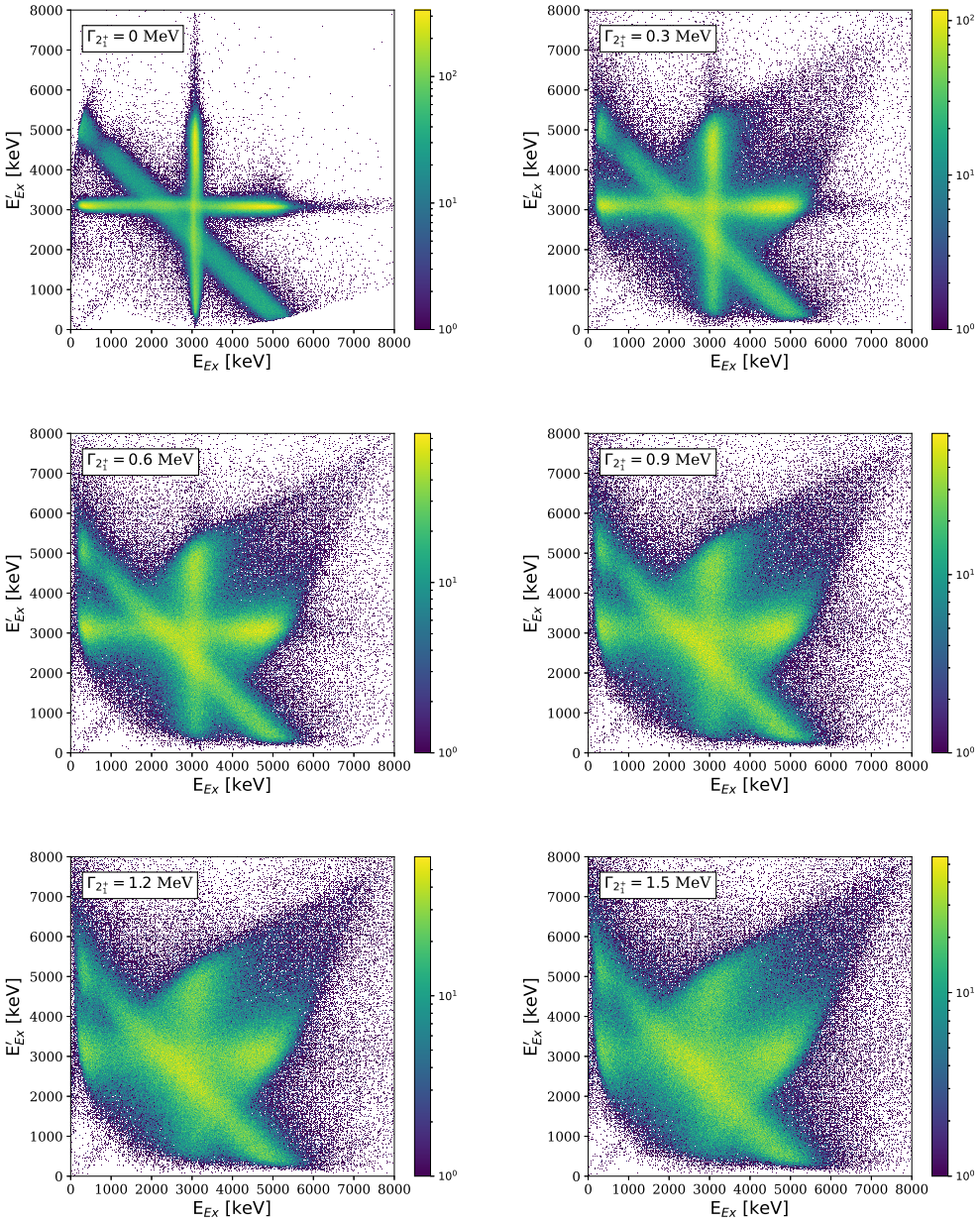

FIGURE 4.6: Dalitz plots of simulations of the γ-delayed 2α breakup for $\Gamma_{2_1^+}$ = 0-1.5 MeV. The two axis show the excitation energy calculated with one of the three combinatory pairs.

2-10 MeV (The accelerator at CMAM is a 5 MV tandem accelerator which can accelerate ions twice, meaning that it can maximally produce 10 MeV beams). Although not directly relevant to the CMAM experiment due to the different setups, this will still provide some insight into choosing an optimal beam energy.

Additionally, code was written that can perform multiple simulations using simX, varying some setup- or beam-related parameters between each simulation. These parameters included: (1) the beam energy, (2) the z coordinate of the SU and SD, (3), the z coordinate of the Det1 and Det2, (4) the x coordinate of the Det1 and Det2, and (5) the angle of the Det1 and Det2 relative to the beam (coordinates are defined in Figure 3.5). The aim was to see if changes in the setup would result in significant changes in detector efficiency.

4.5 Results

In this section, the outcomes of this chapter are presented, starting with the derived γ spectra, followed by the results on the detector efficiency.

4.5.1 γ spectra

Including decay through 2_3^+ only

As an example of the particle identification method, the kinematic curve of all three α particles is displayed in Figure 4.7 for the simulation of the γ-delayed 2α breakup via the 2_3^+ state and with $E_d = 2$ MeV. The primary particles are evident at the expected $E_\alpha^{CM} = 1.7$ MeV. By applying the primary particle identification method, the kinematic curve of primary particles is also plotted in Figure 4.7. It looks reasonable with the small spread originating from the 74 keV decay width of the 2_3^+ state.

The calculated γ spectrum using the formula in Equation (4.6) with $E_d = 2$ MeV is displayed in Figure 4.8 along with the theoretical values from the simulation. The figure also includes a plot of the residual between the two distributions, normalized by the error, $\sqrt{N}$. The γ spectrum for $E_d = 7.5$ MeV is presented in Figure 4.9.

A one-to-one correspondence exists between the normalized residuals and the number of standard deviations the deduced distribution is from the theoretical one. Consequently, if the only source of uncertainty was statistical, the

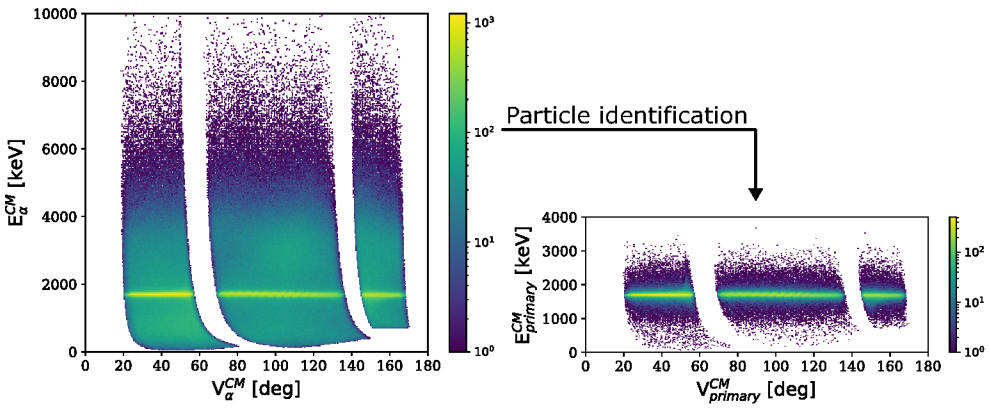

FIGURE 4.7: (Left) Center of mass kinematic curves of all three α particles for the γ-delayed 2α breakup through the 2_3^+ state with $E_d = 2$ MeV. The large amount of data at $E_\alpha^{CM} = 1.7$ MeV are the primary particles. (Right) Center of mass kinematic curve of the primary particles.

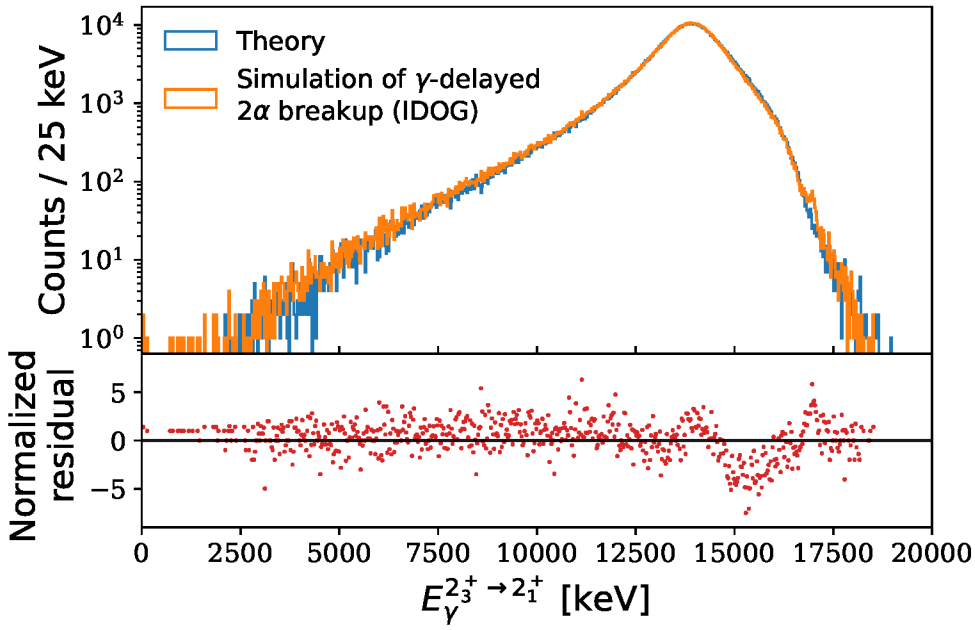

FIGURE 4.8: The γ spectrum for the $2_3^+ \to 2_1^+$ decay with $E_d = 2$ MeV deduced with the IDOG method, along with the theoretical distribution. The normalized residual between the two distributions is also displayed.

normalized residuals would follow a normal distribution centered at zero with a standard deviation of 1. The results will be further discussed in Section 4.6.

Including decay through both 2_3^+ and 2_2^+

In Figure 4.10, the kinematic curve is presented for the case where the γ-delayed 2α breakup can occur through both the 2_2^+ and 2_3^+ states, with $E_d = 2$

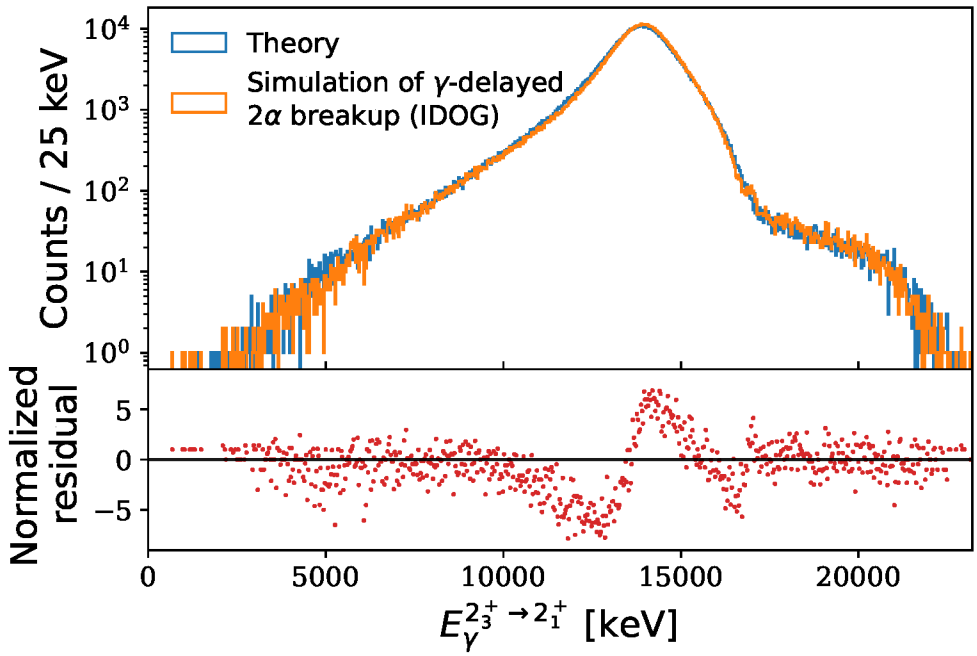

FIGURE 4.9: The γ spectrum for the $2_3^+ \to 2_1^+$ decay with $E_d = 7.5$ MeV deduced with the IDOG method, along with the theoretical distribution. The normalized residual between the two distributions is also displayed.

MeV. The primary particle identification and separation of events through the two states in the isospin doublet are also shown in the same figure. Out of the events assigned to 2_3^+, 12% actually came from 2_2^+, while the opposite is 17%. For $E_d = 7.5$ MeV, the values were 17% and 19%, respectively. The γ spectra from the two states are displayed in Figure 4.11 for $E_d = 2$ MeV, and in Figure 4.12 for $E_d = 7.5$ MeV.

Note that the high-energy tail in the γ spectra of 2_2^+ is missing, as it corresponds to low-energy particles which are always assigned to 2_3^+, as seen in Figure 4.10. As a result, the high-energy tail in the γ spectrum of 2_3^+ is enhanced.

4.5.2 Detector efficiency

A total of 41 simulations of the γ-delayed 2α breakup via 2_3^+ were conducted with the same conditions as described in Section 4.2. In Figure 4.13, the efficiency of detecting three-particle events is shown as a function of the deuterium beam energy. 1.3 percentage points separates the minimum ($E_d = 3.8$ MeV) and maximum ($E_d = 10$ MeV) detector efficiency, and corresponds to a 15% difference.

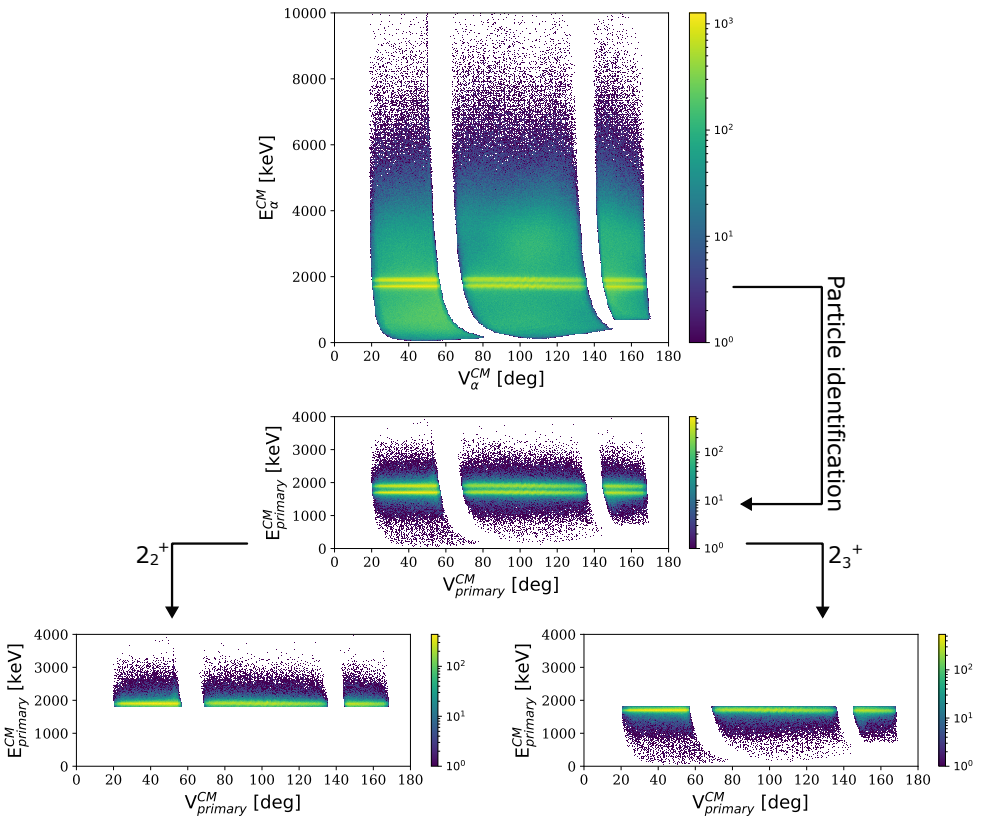

FIGURE 4.10: (Top) Center of mass kinematic curves of all three α particles for the γ-delayed 2α breakup through the 2_3^+ state with $E_d = 2$ MeV. The data at $E_\alpha^{CM} = 1.7$ MeV and 1.9 MeV is the primary particles of the decay via 2_3^+ and 2_2^+, respectively. (Middle) Center of mass kinematic curve of the primary particles. (Bottom) The separation of the primary particles going through 2_3^+ and those going through 2_2^+.

As the beam energy increases, the center of mass moves faster in the beam direction, causing the emitted particle to be emitted at more forward angles in the laboratory frame. This may explain the small drop in detector efficiency from 2-4 MeV, due to a higher chance of the particle being emitted into the space between the Det1/Det2 detectors and the SD. The subsequent increase in efficiency corresponds to the particle becoming more forward, increasing the likelihood of detection in the SD.

The results indicate that choosing the right beam energy can lead to a small improvement in efficiency. The optimal beam energy will vary based on the setup and its solid angle coverage, particularly in the forward direction. However, the simulations of the detector efficiency for different setup configurations showed that increasing coverage at forwarded angles at the expense of total coverage was not found to be beneficial. It seems like when searching for

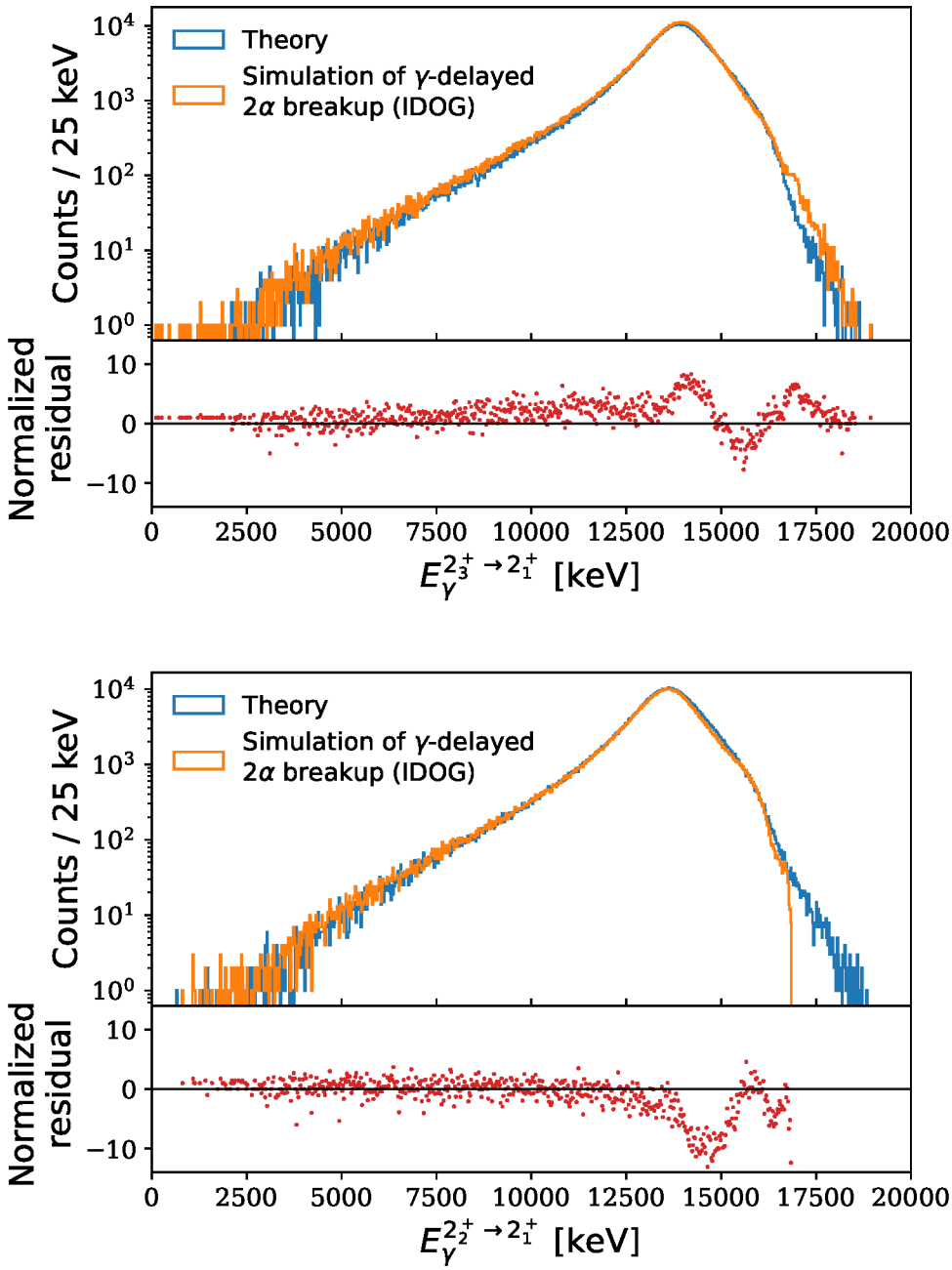

FIGURE 4.11: (Top) The γ spectrum for the $2_3^+ \to 2_1^+$ decay and (Bottom) the γ spectrum for the $2_2^+ \to 2_1^+$ decay with $E_d = 2$ MeV deduced with the IDOG method, along with the theoretical distributions. The normalized residual between the two distributions is also displayed.

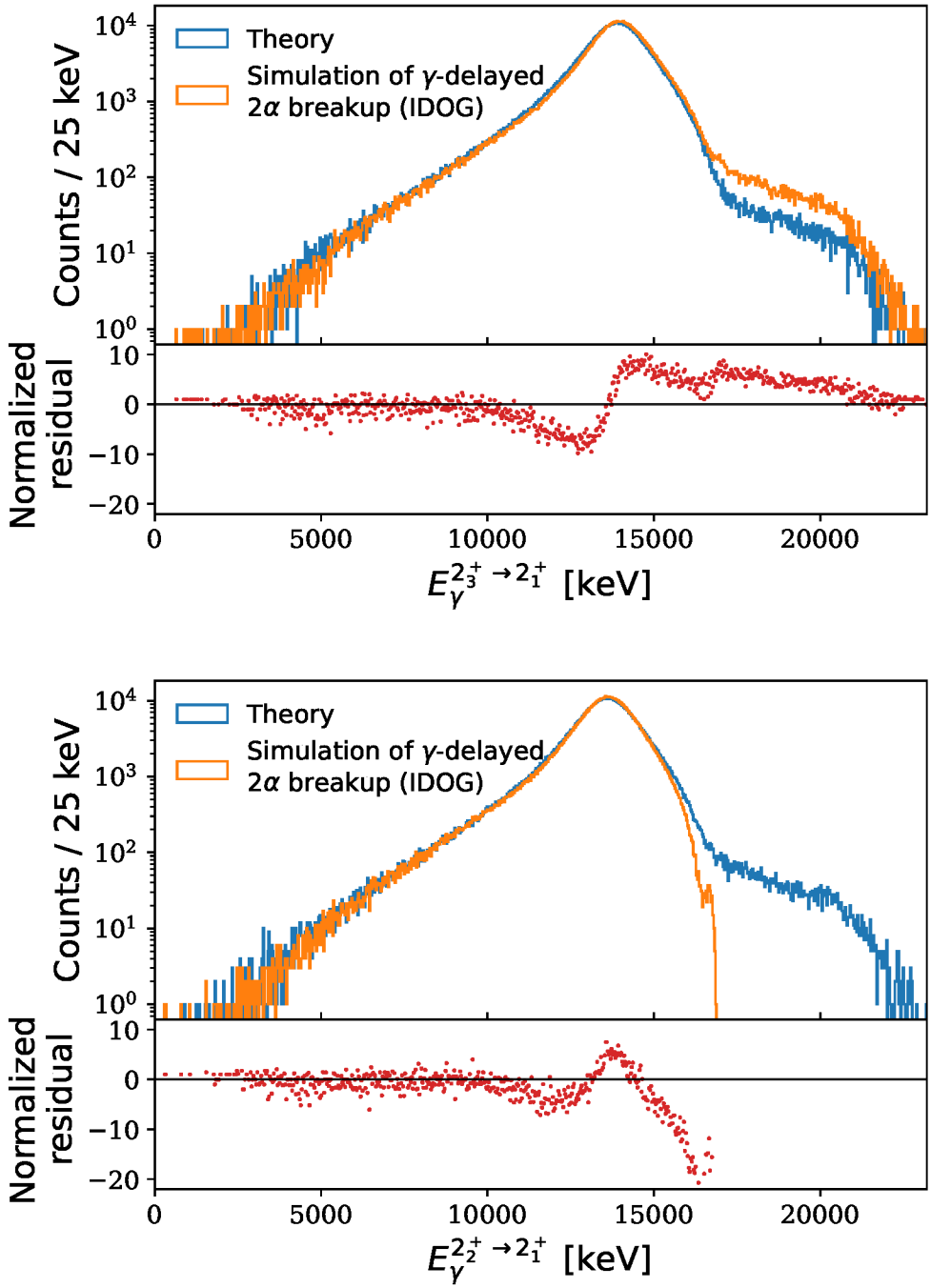

FIGURE 4.12: (Top) The γ spectrum for the $2_3^+ \to 2_1^+$ decay and (Bottom) the γ spectrum for the $2_2^+ \to 2_1^+$ decay with $E_d = 7.5$ MeV deduced with the IDOG method, along with the theoretical distributions. The normalized residual between the two distributions is also displayed.

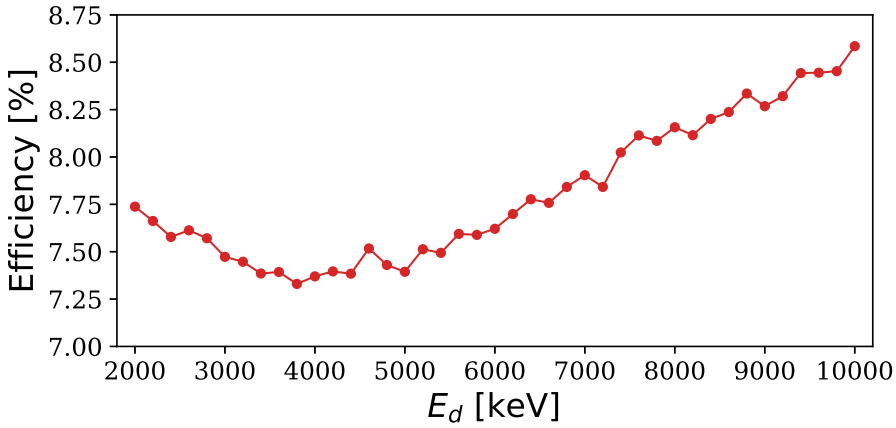

FIGURE 4.13: The efficiency of detecting γ-delayed 2α events via 2_3^+ in complete kinematics as a function of the laboratory deuterium beam energy.

three-particle events, total solid angle coverage is the most crucial aspect of the setup.

Assuming 10% efficiency in detecting γ-delayed 2α breakup in complete kinematics, with a cross section of 10mb and a beam current of 1nA, we calculate the population of one of the isospin doublet states per unit time to be 1731 events/s (calculation explained briefly in Appendix B). The radiative decay width of the isospin doublet to the 2_1^+ state is 2.8 eV [33], meaning that if we take the 2_3^+ state as an example with $\Gamma = 74$ keV, we would expect to detect one γ-delayed 2α breakup event every 15s. Consequently, over the course of three days, we estimate to measure on the order of about 10^4 of these events, similar to the number used in the work of Munch et al. [13].

4.6 Discussion

The results shown in Figure 4.8 and Figure 4.9 exhibit a much closer match with the theoretical results when compared to those presented in Figure 4.11 and Figure 4.12. This discrepancy can be attributed to the possibility of incorrect assignment of the doublet state through which an event occurred, which impacts the final spectra in the latter case. As the latter scenario is a closer reflection of reality, it is crucial to take into account the potential for such incorrect assignments when future studies will attempt to apply the IDOG method to the experimental data from the ^{10}B(d,α)^{8}Be at CMAM.

Nevertheless, the normalized residuals show that the spectra generated by the IDOG method and the theoretical spectra are not from the same distribution.

If there were only statistical uncertainties, 68% should be within one standard deviation which is not what we observe. Instead, we observe some swinging tendency in the residuals, especially near the main peak. In particular, when both doublet states are considered, the deduced γ spectra can deviate from the theoretical distribution by up to ten standard deviations Therefore, there are evident systematic uncertainties present.

The main source of these systematic uncertainties is likely from the energy broadening due to energy loss corrections and response functions, which ultimately blur out the γ spectrum. As a result, the IDOG method is expected to perform poorly in deducing the γ spectrum in steep regions. This is exactly what is seen in the residuals in the steep regions near the main peak.

Additionally, another source of systematic uncertainty is the method used for particle identification. As previously stated, this method may make biased incorrect assignments of primary particles. Specifically, events with primary particles ending up in the tails of any of the doublet states are more prone to having their particle assignments misinterpreted.

In the low-energy region, the IDOG method exhibits optimal performance. Here, the normalized residuals are primarily influenced by statistical uncertainties. This makes it a significant improvement compared to the spectra measured with a NaI detector in Figure 4.2, which were not able to go beyond 10 MeV due to the increasing uncertainties. Measuring the low-energy region using the IDOG method would therefore be a noteworthy advancement.

To address the discrepancy mentioned above, an R-matrix fit of an experimentally deduced γ spectrum would require iteration to adjust parameters to match simulations. Another option is to remove the energy broadening effects through a simulation-based deconvolution, but this would be difficult due to the response potentially being affected by numerous factors such as the detector and strip hit, particle energy, and angle of incidence. This is further complicated by the fact that the spectrum is deduced based on measurements from three particles, each with varying energies, angles, etc., and therefore subject to different response functions.

The results presented here suggest that the use of the IDOG method in the ^{10}B(d,α)^{8}Be experiment could bring substantial enhancements to the γ spectra of the isospin doublet. Particularly, it is anticipated to offer a novel understanding of the low-energy region of the spectra.

Chapter 5

Conclusion

The main focus of this thesis has been on using the IDOG method to indirectly detect electromagnetic transitions involving broad unbound state in γ-delayed particle emissions from ^{16}O and ^{8}Be.

In the ^{15}N(p,α)^{12}C experiments, the main goal was to determine if the 9.59 (1^-) and 9.84 (2^+) MeV states could be populated through the γ-delayed α decay of the 12.97 (2^-) and 13.09 (1^-) MeV states in ^{16}O, as this would help constraining the extrapolation of the E1 but most importantly also the E2 component of the ^{12}C(α,γ)^{16}O reaction rate. However, no significant amount of γ-delayed α-decay was observed to any of the natural parity states above the α separation energy, so instead upper limits on the radiative decay widths were computed through Monte Carlo simulations. In particular, it was possible to set sensible 90% CL upper limits on the radiative decay widths for the 12.97 $\rightarrow$ 9.84, 12.97 $\rightarrow$ 9.59, 13.09 $\rightarrow$ 9.84, and 13.09 $\rightarrow$ 9.59 dipole transitions of 7.5 meV, 21 meV, 0.12 eV, and 0.25 eV, respectively, which there exist no literature values of so far. These limits were up to four orders of magnitude smaller than expected by the Weisskopf estimates and suggested the need for more precise theoretical calculations and a repetition of the experiment with longer measurement time to significantly increase the sensitivity.

To determine the feasibility of using the IDOG method in extracting the $M1$ radiative decay width of the transition from the isospin doublet to the broad 3.0 MeV state in a ^{10}B(d,α)^{8}Be experiment, Monte Carlo simulations of the γ-delayed 2α breakup were carried out at two different deuterium beam energies. By comparing the γ spectra produced by the IDOG method to theoretical ones,

the simulations revealed systematic uncertainties associated with energy loss correction and response function. These findings provide a foundation for extracting a trustworthy R-matrix parameterization of the γ spectrum from the ^{10}B(d,α)^{8}Be experiment, which must be iteratively adjusted to address the discrepancies highlighted in this work. The IDOG method also showed the potential to offer a new insight into the low-energy region of the spectra where conventional γ spectroscopy is not capable of providing reliable results.

Bibliography

[1] Kenneth S Krane. *Introductory nuclear physics*. John Wiley & Sons, 1991.

[2] B.R. Martin and G. Shaw. *Nuclear and particle physics: an introduction*. John Wiley & Sons, 2019.

[3] A. Obertelli and H. Sagawa. "Nuclear Structure Theory". In: *Modern Nuclear Physics*. Springer, 2021, pp. 93–185.

[4] K Ikeda, N. Takigawa, and H. Horiuchi. "The systematic structure-change into the molecule-like structures in the self-conjugate 4n nuclei". In: *Progress of Theoretical Physics Supplement* 68 (1968), pp. 464–475.

[5] S.C. Pieper and R.B. Wiringa. "Quantum Monte Carlo calculations of light nuclei". In: *Annual Review of Nuclear and Particle Science* 51.1 (2001), pp. 53–90.

[6] B.R. Barrett, P. Navrátil, and J.P. Vary. "Ab initio no core shell model". In: *Progress in Particle and Nuclear Physics* 69 (2013), pp. 131–181.

[7] A.M. Lane and R.G. Thomas. "R-matrix theory of nuclear reactions". In: *Reviews of Modern Physics* 30.2 (1958), p. 257.

[8] D. Zahnow et al. "The S(E) factor of ^{7}Li(p,γ)^{8}Be and consequences for S(E) extrapolation in ^{7}Be(p,γ_0)^{8}B". In: *Zeitschrift für Physik A Hadrons and Nuclei* 351.2 (1995), pp. 229–236.

[9] H. Fynbo. *ERC Starting Grant. Research proposal (Part B section 2(B2))*. 2012.

[10] M. Alcorta et al. "A complete kinematics approach to study multi-particle final state reactions". In: *Nuclear Instruments and Methods in Physics Research Section A: Accelerators, Spectrometers, Detectors and Associated Equipment* 605.3 (2009), pp. 318–325.

[11] O.S. Kirsebom et al. “Observation of γ-delayed 3α breakup of the 15.11 and 12.71 MeV states in ^{12}C”. In: *Physics Letters B* 680.1 (2009), pp. 44–49.

[12] O.S. Kirsebom et al. “Experimental study of the ^{11}B(p,3α)γ reaction at E_p = 0.5-2.7 MeV”. In: *The European Physical Journal A* 56.7 (2020), pp. 1–10.

[13] M. Munch et al. “Measurement of the full excitation spectrum of the ^{7}Li(p,γ)$\alpha\alpha$ reaction at 441 keV”. In: *Physics Letters B* 782 (2018), pp. 779–784.

[14] R.J. Deboer et al. “The ^{12}C(α,γ)^{16}O reaction and its implications for stellar helium burning”. In: *Reviews of Modern Physics* 89.3 (2017), p. 035007.

[15] F. Hoyle. “On Nuclear Reactions Occuring in Very Hot STARS. I. the Synthesis of Elements from Carbon to Nickel.” In: *The Astrophysical Journal Supplement Series* 1 (1954), p. 121.

[16] D. Schürmann et al. “First direct measurement of the total cross-section of ^{12}C(α,γ)^{16}O”. In: *The European Physical Journal A-Hadrons and Nuclei* 26.2 (2005), pp. 301–305.

[17] L. Buchmann et al. “β-delayed α spectrum of ^{16}N and the ^{12}C(α,γ)^{16}O cross section at low energies”. In: *Phys. Rev. Lett.* 70 (6 Feb. 1993), pp. 726–729.

[18] D.H. Wilkinson. *ISOSPIN IN NUCLEAR PHYSICS.* 1969.

[19] J. Refsgaard et al. “Measurement of the branching ratio for β-delayed α decay of ^{16}N”. In: *Physics Letters B* 752 (2016), pp. 296–301.

[20] D.R. Tilley, H.R. Weller, and C.M. Cheves. “Energy levels of light nuclei A= 16–17”. In: *Nuclear Physics A* 564.1 (1993), pp. 1–183.

[21] S. Meijer, J.J. Smit, and A. Girodet. “Comparison of the Breakdown Strength of N2, CO2 and SF6 using the Extended Up-and-Down Method”. In: (2006), pp. 653–656.

[22] *Micron Semiconductor Ltd.* `http://www.micronsemiconductor.co.uk`. Accessed: 2022-10-06.

[23] G.F. Knoll. *Radiation detection and measurement*. John Wiley & Sons, 2010.

[24] *Rene Brun and Fons Rademakers, ROOT - An Object Oriented Data Analysis Framework*. `https://root.cern`. Accessed: 2021-01-02.

[25] *AUSAlib - Aarhus University Subatomic library*. `https://gitlab.au.dk/ausa`. Accessed: 2021-01-02.

[26] *Gitlab of the ucesb program*. `https://git.chalmers.se/expsubphys/ucesb`. Accessed: 2021-01-02.

[27] *SRIM - The Stopping and Range of Ions in Matter*. `http://www.srim.org/`. Accessed: 2023-02-07.

[28] National Nuclear Data Center (NNDC) at Brookhaven National Laboratory. *NuDat 3*. `https://www.nndc.bnl.gov/nudat3/`. Accessed: 2021-01-08.

[29] O. Behnke, K. Kröninger, G. Schott, and T. Schörner-Sadenius. *Data analysis in high energy physics: a practical guide to statistical methods*. John Wiley & Sons, 2013.

[30] O.S. Kirsebom et al. "Precise and accurate determination of the ^{8}B decay spectrum". In: *Physical Review C* 83 (2011), p. 065802.

[31] T. Roger et al. "Precise Determination of the Unperturbed ^{8}B Neutrino Spectrum". In: *Physical Review Letters* 108.16 (2012), p. 162502.

[32] D.R. Tilley et al. "Energy levels of light nuclei A= 8, 9, 10". In: *Nuclear Physics A* 745.3-4 (2004), pp. 155–362.

[33] L. De Braeckeleer et al. "Radiative decays of the 16.6 and 16.9 MeV states in ^{8}Be and tests of the conservation of the vector current in the A=8 multiplet". In: *Physical Review C* 51.5 (1995), p. 2778.

[34] X.B. Wang and A.C. Hayes. "Weak magnetism correction to allowed β decay for reactor antineutrino spectra". In: *Physical Review C* 95.6 (2017), p. 064313.

[35] W.D. Callender and C.P. Browne. "Isobaric Spin Doublets in ^{8}Be Excited with the ^{10}B(d,α)^{8}Be Reaction". In: *Physical Review C* 2.1 (1970), p. 1.

Appendix A

A.1 Similar plots for the 1028 keV experiment

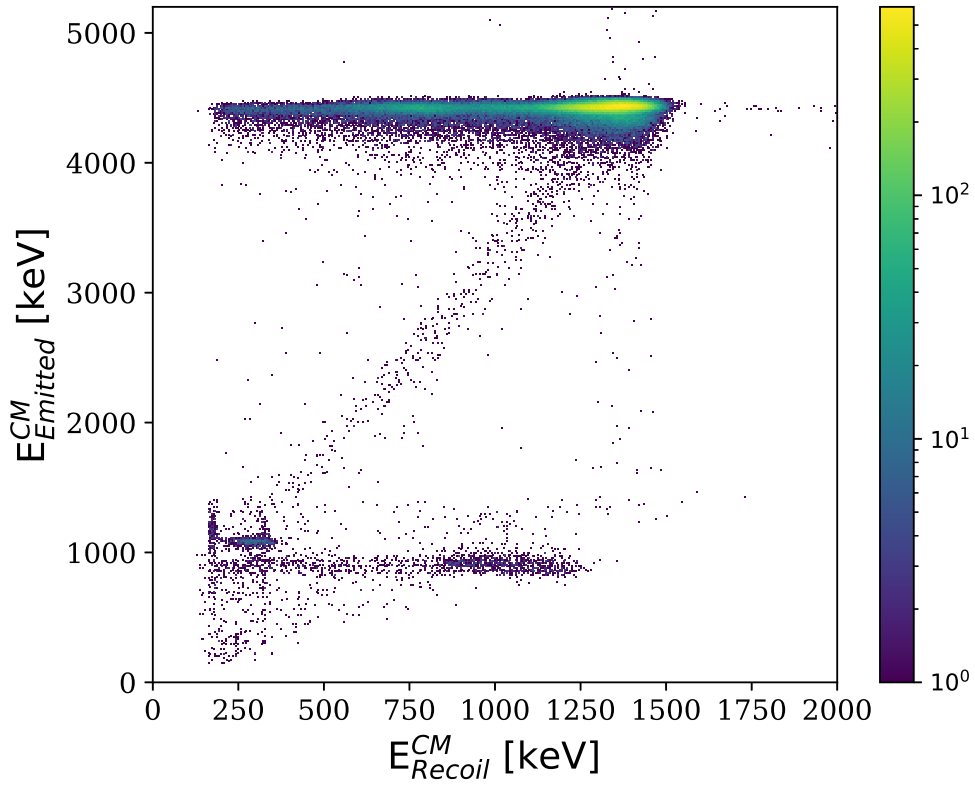

Figure A.1: The center of mass energy of the emitted particle plotted against the energy of the recoil particle for the 1028 keV experiment.

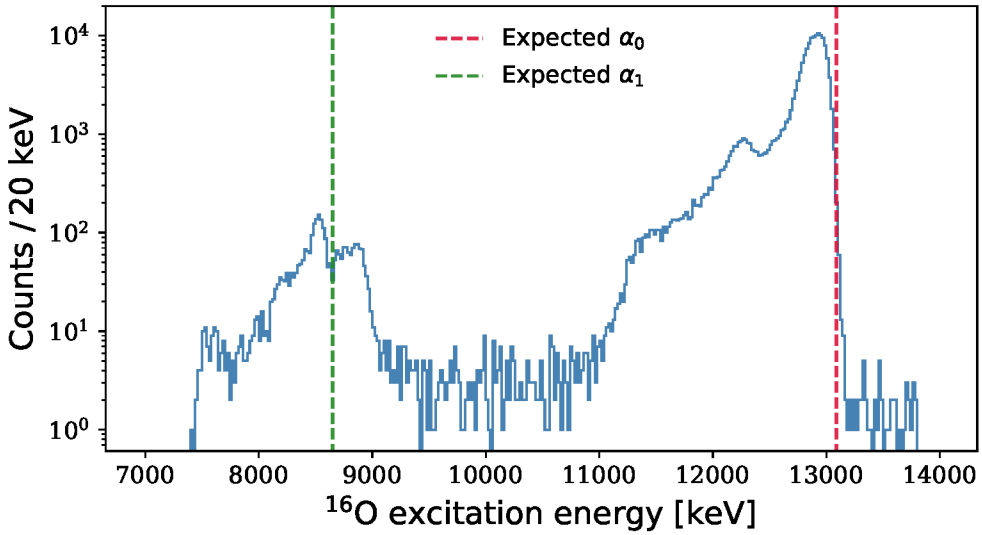

FIGURE A.2: The excitation spectrum of the 1028 keV experiment. The expected positions of the α_0 and α_1 peaks are shown.

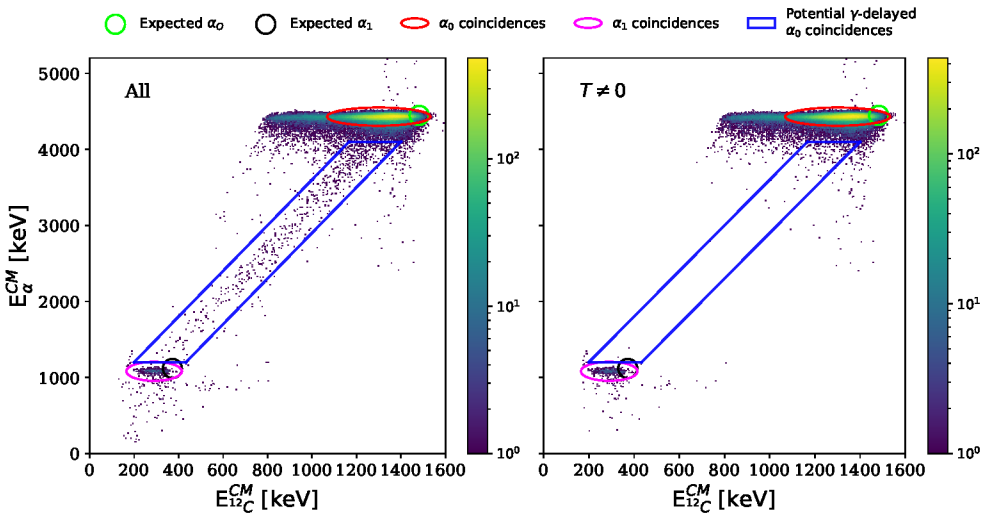

FIGURE A.3: The center of mass energy of the α plotted against the energy of the ^{12}C nucleus for All (left) and T $\neq$ 0 (right) in the 1028 keV experiment. Expected values for α_0 and α_1 decays are indicated with circles, while the actual peaks are indicated with ellipses. The data within the blue box are potential candidates of γ-delayed α_0-coincidences

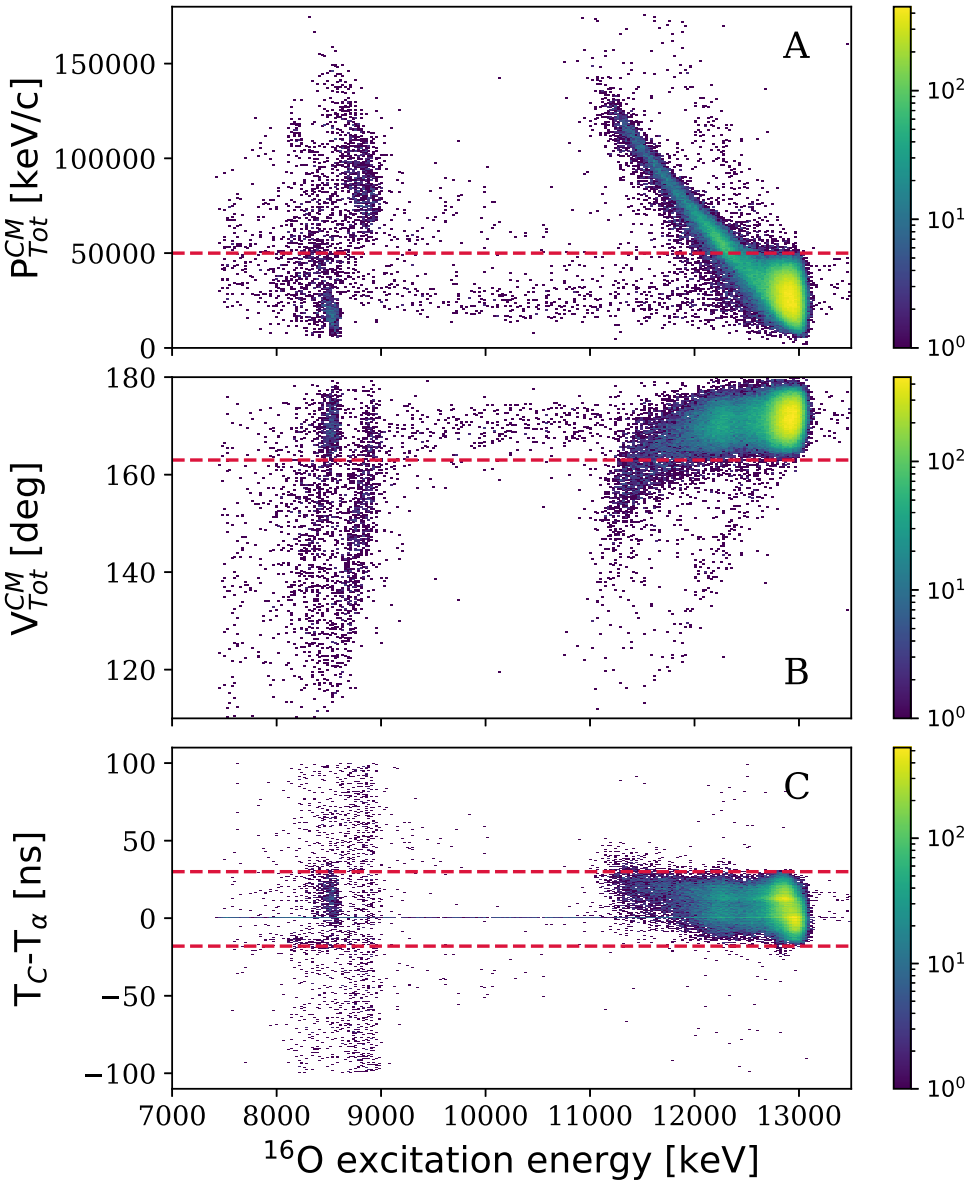

FIGURE A.4: (A) The total center of mass momentum, (B) total angle in the center of mass, and (C) the detection time difference plotted against the excitation energy in ^{16}O for the 1028 keV experiment. The dotted red lines represent the imposed cut.

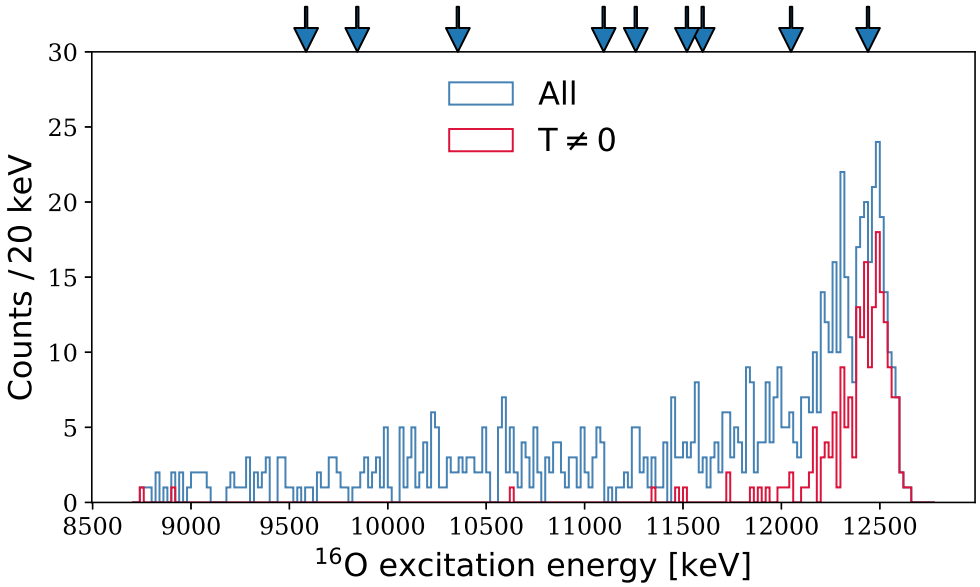

FIGURE A.5: The excitation spectrum of the γ-delayed α_0 candidates for the two cases in the 1028 keV experiment. The arrows indicates the states in Table 3.1.

A.2 Reaction file for γ-delayed α decay of ^{16}O

SCRIPT A.1: Example of a reaction.simX file used in simulating γ-delayed α decay

```
1  beam: p
2  target: N15
3  -> {
4       O16 Ex: 12.9686 MeV G0: 1.34keV
5       -> {
6            weight: BW*GAMMA
7            L: 1
8            g
9            O16 Ex: 12.440MeV G0: 91keV
10           -> {
11                weight: PEN
12                a
13                C12 Ex: 0MeV
14           }
15      }
16 }
```

Appendix B

B.1 Reaction file for γ-delayed 2α breakup

Script B.1: Example of a reaction.simX file used in simulating the γ-delayed 2α breakup through the 2_3^+ state

```
beam: d
target: B10
-> {
     weight: BW
     a
     Be8 Ex: 16.922 MeV G0: 74keV
     -> {
          weight: BW*GAMMA
          L: 1
          g
          Be8 Ex: 3.03MeV G0: 1.5keV
          -> {
               weight: PEN
               a
               a
          }
     }
}
```

B.2 Derivation of the α particle energy equations

We will here show the derivation of the equations for the α particle energies (Equation (4.3)).

In the first sequential step, the energy available is Q_1 and the center of mass beam energy is given by

$$E_d^{CM} = E_d\left(1 - \frac{m_d}{m_d + m_{^{10}\mathrm{B}}}\right) = \frac{5}{6}E_d. \tag{B.1}$$

Imposing energy conservation and using that $E = p^2/2m$ gives

$$\begin{aligned} Q_1 + \frac{5}{6}E_d = E_1 + E_{\mathrm{Be}} = E_1 + \frac{p_{\mathrm{Be}}^2}{2m_{\mathrm{Be}}} &= E_1 + \frac{(-p_1)^2}{2(2m_\alpha)} = E_1 + \frac{1}{2}E_1 = \frac{3}{2}E_1 \\ \rightarrow \quad E_1 = \frac{2}{3}Q_1 + \frac{5}{9}E_d, &\quad E_{\mathrm{Be}} = \frac{1}{2}E_1, \end{aligned} \tag{B.2}$$

where we used that there is conservation of momentum in the center of mass so $p_1 + p_{^8\mathrm{Be}} = 0$.

In the second sequential step, the energy available in the center of mass is Q_2 and $E_{\mathrm{Be}} = \frac{1}{2}E_1 = \frac{1}{3}Q_1 + \frac{5}{18}E_d$. Momentum conservation states that $p_2' + p_3' = 0$ in the center of mass of ^{8}Be (denoted with a prime). Since the masses of the two decay products are the same, energy conservation implies that $E_2' = E_3' = Q_2/2$. Boosting to the center of mass then gives

$$\begin{aligned} E_2 &= \frac{1}{2}m_\alpha(v' + v_{\mathrm{Be}})^2 \\ &= \frac{1}{2}m_\alpha v_{\mathrm{Be}}^2 + \frac{1}{2}m_\alpha v'^2 + m_\alpha v' v_{\mathrm{Be}} \\ &= \frac{1}{2}E_{\mathrm{Be}}^2 + E_2' + m_\alpha \cos\theta \sqrt{\frac{2E_2'}{m_\alpha}}\sqrt{\frac{2E_{\mathrm{Be}}}{2m_\alpha}} \\ &= \frac{1}{4}E_1 + \frac{1}{2}Q_2 + \cos\theta\sqrt{\frac{2Q_2}{2}}\sqrt{\frac{E_1}{2}} \\ &= \frac{1}{4}E_1 + \frac{1}{2}Q_2 + \cos\theta\sqrt{\frac{E_1 Q_2}{2}}. \end{aligned} \tag{B.3}$$

Finally, energy conservation in the center of mass gives the energy of the

second decay product

$$\begin{aligned} E_3 &= E_{\mathrm{Be}} + Q_2 - E_2 \\ &= \frac{1}{2}E_1 + Q_2 - \left(\frac{1}{4}E_1 + \frac{1}{2}Q_2 + \cos\theta\sqrt{\frac{E_1 Q_2}{2}}\right) \\ &= \frac{1}{4}E_1 + \frac{1}{2}Q_2 - \cos\theta\sqrt{\frac{E_1 Q_2}{2}}. \end{aligned} \tag{B.4}$$

B.3 Calculation of number of population per unit time

We will here show the derivation of the equations for the number of populations of the isospin doublet.

The reaction cross section σ is defined as the ratio of the rate of reactions N_r/t to the product of the number of incident beam particles per unit time N_b/t and the number of target nuclei per unit area N_t/A [1]. Thus we express N_r/t as

$$\frac{N_r}{t} = \frac{N_b}{t}\frac{N_t}{A}\sigma. \tag{B.5}$$

The number of incident beam particles can be expressed as I/qe, where I is the electric current of the beam and q is the electrical charge of the beam particle. The number of target nuclei per unit area is the product of the target density, its thickness, and the number of nuclei per mass unit, $\rho d N_A/M$, where N_A is Avogadro's constant and M is the molar mass. Finally, to obtain the number of detected reactions per time unit, we must multiply by the detection efficiency ϵ. Hence, the final equation is

$$\frac{N_r}{t} = \frac{I}{qe}\rho d\frac{N_A}{M}\sigma\epsilon. \tag{B.6}$$

In the case of $I = 1\mathrm{nA}$, $\sigma = 10mb = 10^{-30}m^2$ and $\epsilon = 0.1$, the rate is

$$\begin{aligned} \frac{N_r}{t} &= \frac{10^{-9}\frac{C}{s}}{1\cdot 1.6\times 10^{-19}C}\cdot 2.3\times 10^6\frac{g}{m^3}\cdot 20\times 10^{-6}m\cdot\frac{6.02\times 10^{23}mol^{-1}}{10\frac{g}{mol}}\cdot 10^{-30}m^2\cdot 0.1 \\ &= 1731s^{-1}. \end{aligned} \tag{B.7}$$